Chemical Engineering Journal 500 (2024) 157300

Contents lists available at ScienceDirect

Chemical Engineering Journal

journal homepage: www.elsevier.com/locate/cej

The ROS-responsive FA@Ni@HA hydrogel promotes infected wound healing in DIO mice through endogenous antimicrobial peptides and macrophage recruitment

Weixian Hu [a,b,1], Yanzhi Zhao [a,b,1], Shengming Zhang [a,b,1], Yue An [c,1], Samuel Knoedler [d,e], Adriana Christine Panayi [d,f], Doha Obed [g], Bong-Sung Kim [h], Kangkang Zha [a,b], Wenqian Zhang [a,b], Yixin Hu [i], Bobin Mi [a,b], Qian Feng [c,*], Hankun Hu [i,j,k,*], Yun Sun [l,*], Guohui Liu [a,b,*]

[a] Department of Orthopedics, Union Hospital, Tongji Medical College, Huazhong University of Science and Technology, Wuhan 430022, China
[b] Hubei Province Key Laboratory of Oral and Maxillofacial Development and Regeneration, Wuhan 430022, China
[c] Key Laboratory of Biorheological Science and Technology, Ministry of Education, College of Bioengineering, Chongqing University, Chongqing 400044, China
[d] Division of Plastic Surgery, Brigham and Women's Hospital, Harvard Medical School, Boston, MA 02152, USA
[e] Institute of Regenerative Biology and Medicine, Helmholtz Zentrum München, Max-Lebsche-Platz 31, 81377 Munich, Germany
[f] Department of Hand, Plastic and Reconstructive Surgery, Microsurgery, Burn Center, BG Trauma Center Ludwigshafen, University of Heidelberg, Ludwig-Guttmann-Strasse 13, 67071 Ludwigshafen/Rhine, Germany
[g] Department of Plastic, Aesthetic, Hand and Reconstructive Surgery, Hannover Medical School, Hannover, Germany
[h] Department of Plastic Surgery and Hand Surgery, University Hospital Zurich, 8091 Zurich, Switzerland
[i] Department of Pharmacy, Zhongnan Hospital of Wuhan University, School of Pharmaceutical Sciences, Wuhan University, Wuhan 430071, China
[j] Hubei Micro-explore Innovative Pharmaceutical Research Co, Ltd, Wuhan, Hubei 430074, China
[k] Suzhou Organ-on-a-Chip System Science and Technology Co., Ltd, Suzhou, Jiangsu 215000, China
[l] Department of Neurosurgery, Union Hospital, Tongji Medical College, Huazhong University of Science and Technology, 1277 Jiefang Avenue, Wuhan 430022, China

ARTICLE INFO

Keywords:
Infected wound healing
Obesity
Antimicrobial peptides
Macrophage
Adipocytes
Hydrogel

ABSTRACT

In infected wounds, adipocytes play a crucial role in resisting infection. Studies have demonstrated that a lack of adipocytes can reduce the recruitment of macrophages. When wounds are infected, dermal fibroblasts (dFBs) differentiate into adipocytes and produce antimicrobial peptides (AMPs) to combat bacteria. However, in obesity mice, mature adipocytes hinder the adipogenic differentiation of dFBs and the production of AMPs. It is unclear whether promoting lipolysis can restore the function of AMPs secretion. Nickel ion (Ni^{2+}) is known for promoting vascular regeneration and has been widely used in tissue regeneration. Therefore, the ROS-responsive ferulic acid (FA)@Ni@HA hydrogel was developed to promote infected wound healing. FA released from the hydrogel can promote the lipolysis of adipocytes to alleviate the inhibition of mature adipocytes on AMPs secretion from dFBs and enhance macrophage recruitment. Additionally, the loaded Ni^{2+} can stimulate local blood vessel formation, working in conjunction with FA to promote the healing of infected wounds. The results suggest that the use of FA@Ni@HA hydrogel expedites the repair of infected wounds, offering a promising strategy for wound healing.

* Corresponding authors at: Department of Orthopedics, Union Hospital, Tongji Medical College, Huazhong University of Science and Technology, Wuhan 430022, China (G. Liu); Department of Neurosurgery, Union Hospital, Tongji Medical College, Huazhong University of Science and Technology, 1277 Jiefang Avenue, Wuhan 430022(Y. Sun); China Department of Pharmacy, Zhongnan Hospital of Wuhan University, School of Pharmaceutical Sciences, Wuhan University, Wuhan 430071, China (H. Hu); Key Laboratory of Biorheological Science and Technology, Ministry of Education, College of Bioengineering, Chongqing University, Chongqing 400044, China (Q. Feng).
E-mail addresses: qianfeng@cqu.edu.cn (Q. Feng), huhankun@whu.edu.cn (H. Hu), 627224540@qq.com (Y. Sun), liuguohui@hust.edu.cn (G. Liu).
[1] These authors contributed equally to this work.

https://doi.org/10.1016/j.cej.2024.157300
Received 9 September 2024; Received in revised form 21 October 2024; Accepted 30 October 2024
Available online 1 November 2024

1. Introduction

With the continuous increase in wealth, the prevalence of obesity is rapidly increasing, posing a significant global public health concern [1]. Obesity has been found to have a detrimental impact on wound healing, as it can intensify local inflammatory responses, raise the risk of wound infections, and worsen the outcomes of such infections [1–4]. The stages involved in wound healing include hemostasis, inflammation, proliferation, and remodeling. In cases where exogenous microorganisms or bacteria infect the wounds, the inflammatory phase may be prolonged, preventing the transition to the proliferation stage and leading to delayed wound healing [5,6]. Consequently, addressing infected wounds in obese patients has emerged as a crucial area of research. Antimicrobial peptides (AMPs) present a favorable new antibacterial treatment option, exhibiting potent bactericidal effects and a high degree of antibacterial activity, offering a promising solution to the issue of antibiotic resistance [7,8]. These peptides function by binding to and disturbing the negatively charged membranes of microbial cells. Additionally, they hinder the production of essential microbial molecules, including proteins and nucleic acids [9,10]. The immune-based antimicrobial agents hold significant promise for the treatment of infected wounds.

Dermal adipose tissue plays a crucial role in secreting AMPs, serving as a vital defense against pathogen transmission [11]. When Staphylococcus aureus (S.aureus) infects skin, it triggers the differentiation of dermal fibroblasts (dFBs) into adipocytes and expands local dermal adipocytes, leading to increased production of AMPs [12,13]. Interestingly, the number of dermal adipocytes in obesity is inversely related to the ability of wounds to resist infection. Previous studies have shown that diet-induced obesity (DIO) mice inhibit wound healing compared to normal mice [14]. Research indicated that mature adipocytes can impede the differentiation of dFBs into adipocytes and suppress the expression of AMPs [11]. Therefore, enhancing the expression of AMPs could potentially bolster the wound's local anti-infection capabilities.

Lipolysis, the process of breaking down fats in the body, relies on the activity of specific enzymes like adipose triglyceride lipase (ATGL), hormone-sensitive lipase (HSL), and monoacylglycerol lipase [15]. ERK, a key component of the mitogen-activated protein kinase family, is essential for regulating cell signaling pathways and controlling numerous physiological functions [16]. Earlier researches have demonstrated that ERK activation in white adipose tissue can lead to the phosphorylation of HSL, enhancing its lipolytic activity [17,18]. Ferulic acid (FA), a polyphenolic acid known for its anti-inflammatory and antioxidant properties, has shown therapeutic benefits in conditions like cardiovascular disease, cancer, and skin disorders [19,20]. FA has been shown to activate the ERK pathway, thereby promoting lipolysis through HSL phosphorylation [21]. As a result, we hypothesize that FA may alleviate the inhibitory effects of AMPs by enhancing lipolysis in mature adipocytes, potentially aiding in the healing of infectious wounds.

In recent years, there has been a growing focus on the role of macrophages in wound healing [22,23]. After an injury occurs, monocytes travel from the blood to the injured area and transform into M1 macrophages in order to fight off microorganisms [24]. As the initial inflammatory response diminishes, there is a shift in the macrophage population towards M2 macrophages. M2 macrophages are essential in regulating inflammation resolution and facilitating tissue repair [25,26]. Research suggests that the breakdown of adipocytes is paramount for macrophage recruitment, as demonstrated by the inhibited recruitment of macrophages in mice lacking the ATGL gene [27]. This leads us to hypothesize that enhancing adipocytes breakdown can improve macrophage recruitment, working in conjunction with AMPs in the wound environment to enhance the wound's antibacterial capacity. Our results indicated that FA can promote lipolysis by promoting phosphorylation of HSL proteins thereby promoting macrophage recruitment. In DIO mice, the abnormal inflammatory response hinders the transition of the wound environment to the proliferation phase [22]. FA, known for its anti-inflammatory properties, has the ability to promote the transformation of the M2 macrophages during the wound proliferation phase, thereby aiding in wound healing.

Covalent organic frameworks (COFs) represent a class of crystalline porous networks constructed from organic building blocks, offering highly customizable structures and tailored functionality. With high porosity, excellent drug loading capabilities and good biocompatibility, COFs find extensive applications in biomedicine [28,29]. Ni^{2+}, a key trace element, plays a crucial role in promoting VEGF expression by stabilizing hypoxia-inducible factor-1α (HIF-1α), thereby facilitating local revascularization and has been used in tissue regeneration engineering [30,31]. Previous research has demonstrated that loading nanozymes onto COFs effectively inhibits bacterial infections and accelerates wound healing [32,33]. Consequently, our study focused on the design of Ni COF nanoparticles to enhance local blood vessel regeneration.

Hydrogels, which are polymers with 3D hydrophilic network structure formed through physical or chemical cross-linking, are commonly utilized in biomedical engineering for their applicability, biocompatibility, degradability and cell adhesion [34]. The oxidative stress in infected wounds is characterized by a significant increase in the level of reactive oxygen species (ROS) [35]. To address this issue, the ROS-responsive FA@Ni@HA hydrogel was developed. This hydrogel utilizes the dynamic phenylboronic acid ester structure formed by hyaluronic acid, phenylboronic acid (PBA) and polyvinyl alcohol (PVA). The Ni COF nanoparticles and FA loaded in the hydrogel are released in response to ROS. The antibacterial function of FA is achieved by promoting lipolysis to enhance the secretion of AMPs and the recruitment of macrophages. Additionally, it reduces oxidative stress and inflammatory response through its antioxidant and anti-inflammatory properties. Ni^{2+} is considered to promote local vascularization, synergistically improving the local microenvironment and promoting the healing of infected wounds. Furthermore, the effectiveness of the composite hydrogel was evaluated using an infected wound model in DIO mice to assess its therapeutic effects in vivo. The FA@Ni@HA hydrogel unveils a novel antibacterial mechanism of FA and holds promise as a new and effective treatment strategy for infected wounds (Fig. 1).

2. Materials and methods

2.1. Synthesis of HA-PBA

To start, 2 g of hyaluronic acid was dissolved in 200 ml of de-ionized water while being stirred continuously. Then, 1 g of 3-Aminophenylboronic acid hydrochloride and 2 g of 4-(4,6-dimethoxy-1,3,5-triazin-2-yl)-4-methyl-morpholinium chloride (DMTMM) were separately introduced to the solution. The reaction mixtures underwent stirring at room temperature for a period of 72 h. Post-reaction, the mixtures were transferred into dialysis bags with a molecular weight cut-off (MWCO) between 6–8 kDa, and dialysis was carried out against de-ionized water for at least 3 days, with water exchanges occurring thrice daily. Subsequently, the dialyzed solutions underwent freeze-drying for 72 h, and the resulting conjugates were then placed in a desiccator at room temperature for storage.

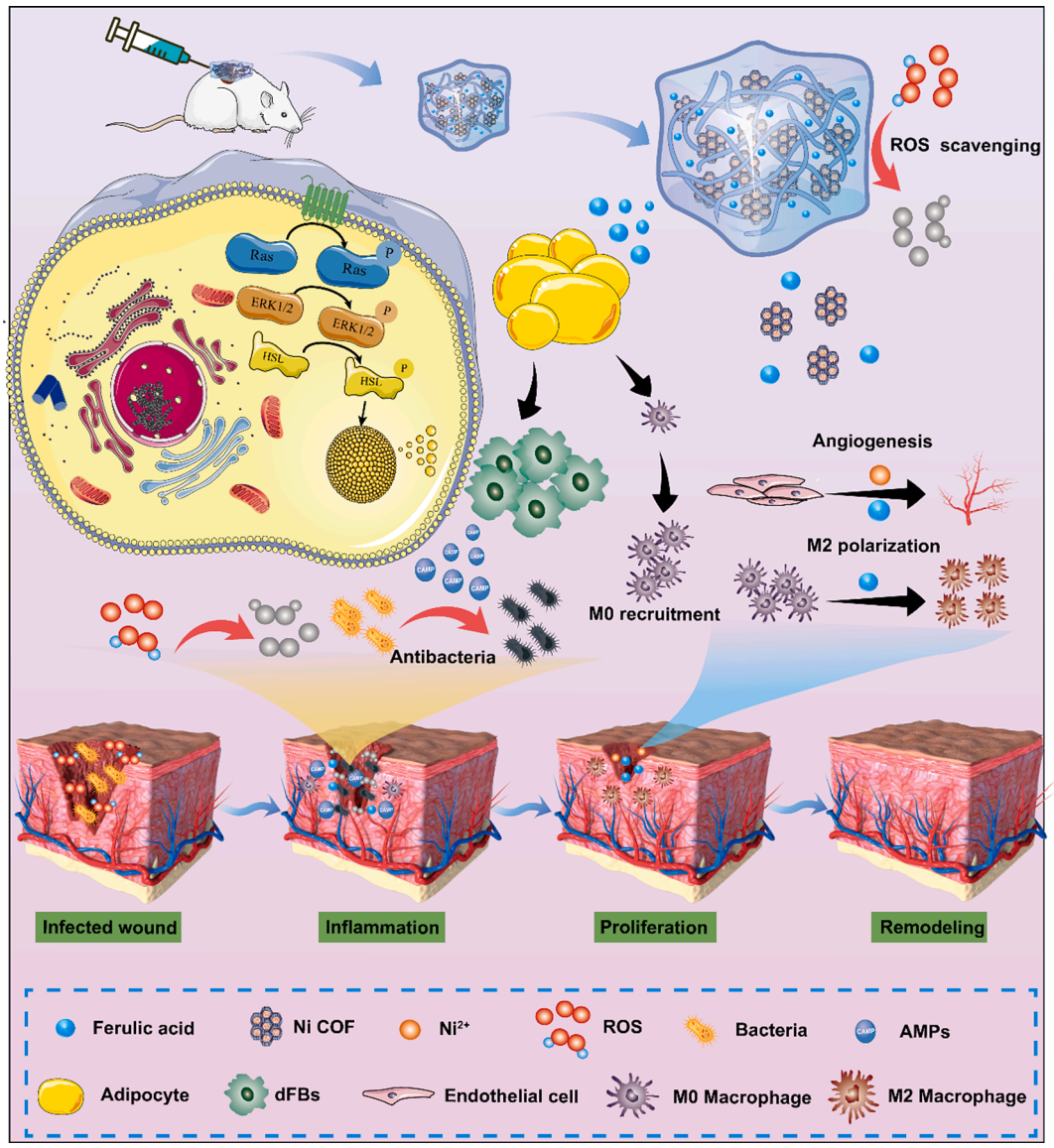

Fig. 1. Schematic diagram of the application of FA@Ni@HA hydrogel in resisting infection and promoting wound healing.

2.2. Synthesis of TpBpy COF

The TpBpy COF was synthesized using the following procedure: 1, 3, 5-triformylphloroglucinol (Tp) (25.2 mg) and 2, 2′-bipyridine-5, 5′-diamine (Bpy) (33.5 mg) were dissolved in a mixture of 1.8 mL dimethylacetamide (DMAc), 0.6 mL o-dichlorobenzene (o-DCB), and 0.24 mL 6.0 M aqueous acetic acid (AcOH). The solution was then rapidly frozen and subjected to three cycles of freeze–pump–thaw. Upon heating the reaction mixture, a deep red material was formed. The resulting material was washed with DMAc, water, and acetone, and then dried to yield the as-synthesized TpBpy COF.

2.3. Synthesis of $NiCl_2$@TpBpy COF

A solution containing 100 mg of TpBpy COF and 129 mg of $NiCl_2$ in 20 mL of methanol (MeOH) was refluxed for 24 h under N_2 gas. The resulting red powder was then washed thrice with MeOH and gathered by vacuum filtration. Finally, the product was dried at a temperature of 80°C in a vacuum oven for 12 h.

2.4. Fabrication of Ni@HA hydrogel and FA@Ni@HA hydrogel

Ni@HA hydrogel was prepared by mixing 180 μl of 10 % HA-PBA, dissolved in phosphate buffer (PBS) at pH 7.4, with 20 μl of 10 % PVA and 2 μl of $NiCl_2$@TpBpy COF solution (1 mM), also dissolved in PBS at pH 7.4 and at room temperature. To load FA into the hydrogel samples, 2 μl of FA solution (10 mM) was mixed directly with 180 μl of 10 % HA-PBA, followed by the addition of 20 μl of 10 % PVA solution and 2 μl of $NiCl_2$@TpBpy COF solution (1 mM) to create drug-loaded hydrogels.

2.5. Morphology characterization

Before lyophilization, the hydrogel was flash-frozen using liquid nitrogen to maintain its structure. Using a scanning electron microscope (SEM), the hydrogel was cross-sectioned following a uniform gold spray. The composite hydrogel's distribution was then examined through energy-dispersive X-ray spectroscopy (EDS).

2.6. Swelling ratio test

The hydrogel's swelling ratios (n = 3) were determined through

gravimetric analysis. The hydrogels were placed in PBS (pH 7.2) for a duration of 24 h. Following the removal of excess liquid using filter paper, the hydrogels that had swelled were weighed (Ws) and subsequently subjected to a 24-hour drying period before being weighed again (Wd). The swelling ratios were then determined utilizing the following formula: Swelling ratio (%) = (Ws − Wd) / Wd × 100.

2.7. ROS response degradation of FA@Ni@HA hydrogels

The degradation of the produced hydrogels was conducted in a PBS buffer and 0.1 mM H_2O_2. Prior to immersion in the solutions, the hydrogels were weighed and the initial weight was recorded as W1. After six hours, the hydrogels were retrieved, weighed and recorded as W2. The degradation ratios were determined utilizing the formula: degradation ratio (%) = (W1 − W2) / W1 × 100.

2.8. FT-IR test

The samples were first blended with potassium bromide at a 1:100 ratio and then formed into pellets. Following this, spectral analysis was conducted using a NICOLET 380 FTIR spectrometer across the 4000—–500 cm^{-1} range, with a resolution of 1 cm^{-1} while operating in transmission mode.

2.9. Hemostasis test

The evaluation of the hydrogel's hemostatic capability was conducted using a hemorrhaging liver model in mice, specifically C57BL/6 males weighing between 25–30 g. To prepare for the procedure, the mice were anesthetized with 10 ml/kg of a 4 % (weight/volume) chloral hydrate solution, procured from Sigma, USA, and administered on a surgical pad to ensure immobilization. Following anesthesia, the liver was accessed through an abdominal incision. A pre-weighed filter paper was strategically placed underneath the liver to subsequently capture and measure blood loss. To induce bleeding in the liver, a 20-gauge needle was inserted at a precise 30° angle, creating a controlled puncture wound. The application of either merocel or the test hydrogels to the bleeding site was carried out. The filter paper was weighed and the results were compared against a control group where no hemostatic treatment was applied post-liver puncture. This process was repeated three times to provide a comprehensive comparison of the hemostatic potential of the tested hydrogels versus the non-treated controls.

2.10. The extraction and culture of dFBs

Primary dermal fibroblasts (dFBs) from mice were extracted using a multi-step digestion process. Initially, mouse skin was treated with dispase, then the dermal tissue was minced into small fragments and further digested using a solution of 2.5 mg/mL Collagenase D and 30 ng/mL DNase I. The resulting cell mixture was passed through a 30 μm filter, followed by treatment with a red blood cell lysis buffer. The isolated dFBs were then cultured in a cell culture medium composed of DMEM, fortified with 10 % fetal bovine serum (FBS) and antibiotics, within a humidified incubator maintained at 37 °C and 5 % CO_2. Only cells at passage 1 were utilized for subsequent experiments. For the induction of adipocyte differentiation, confluent dFBs (two days post-confluence) were switched to an adipogenic differentiation medium containing DMEM, Dexamethasone (2 μM), IBMX (250 μM), Indomethacin (200 μM) and recombinant insulin (10 μg/mL). The differentiation medium was refreshed on day 2, after which it was replaced with a maintenance medium (growth medium with 10 μg/mL recombinant insulin). To set up a co-culture between dFBs and adipocytes, neonatal dFBs were first seeded onto transwell inserts with a 0.4 μm pore size (Corning) and differentiated into mature adipocytes as described above. The inserts with adipocytes were then placed on top of undifferentiated neonatal dFBs in a 6-well plate in adipocytes maintenance medium, with the medium being changed every 3 days. Neonatal dFBs co-cultured with a blank insert without adipocytes were used as a control. After 3–6 days of co-culture, dFBs were collected for analysis. The medium without antibiotics was collected for antimicrobial experiments.

2.11. qRT-PCR analysis

To extract total RNA, TRIzol reagent (Invitrogen, USA) was utilized with subsequent reverse transcription using the RevertAid First Strand cDNA Synthesis kit (Thermo Scientific, USA) following the manufacturer's protocol. For qRT-PCR analysis, the iTaq Universal SYBR Green Supermix (Bio-Rad, USA) was employed in conjunction with the CFX96 Real-Time PCR Detection System (Bio-Rad, USA). The primer sequences utilized were listed below:

	forward	reverse
Mouse β-actin	GTGACGTTGACATCCGTAAAGA	GCCGGACTCATCGTACTCC
Mouse CAMP	GCTGTGGCGGTCACTATCAC	TGTCTAGGGACTGCTGGTTGA
Mouse CCL2	TAAAAACCTGGATCGGAACCAAA	GCATTAGCTTCAGATTTACGGGT
Mouse CCL3	TGTACCATGACACTCTGCAAC	CAACGATGAATTGGCGTGGAA
Mouse CCL4	TTCCTGCTGTTTCTCTTACACCT	CTGTCTGCCTCTTTTGGTCAG
Mouse TNF-α	CAGGCGGTGCCTATGTCTC	CAGGCGGTGCCTATGTCTC

2.12. Western blot

The cells were subjected to lysis with a buffer that included a protease and phosphatase inhibitor cocktail at 1 % concentration (MCE). The proteins were subsequently separated via SDS-PAGE, followed by their transfer onto NC membranes (Millipore). Post-transfer, the NC membranes were blocked for one hour with 5 % skim milk and then incubated overnight at 4 °C with primary antibodies targeting β-actin, CAMP, ERK, HSL, phosphorylated ERK, and phosphorylated HSL (ABclonal, Wuhan). Following this, the blots were exposed to secondary antibodies (Biodragon, AbBox) conjugated with horseradish peroxidase (HRP, Aspen) for one hour at 37°C. Finally, the detection of the proteins was carried out using a chemiluminescence system.

2.13. In vitro antibacterial test

To assess the antibacterial efficacy of various groups, 10 μL of an S. aureus or Escherichia coli (E.coli) bacterial solution (concentration of 1 × 10^7 CFU/mL) was mixed with the supernatants. Following this, 100 μL of the resulting mixture was spread on a nutrient agar plate and incubated for 12 h. After incubation, the colony-forming units (CFUs) were counted. Bacterial viability was calculated using the following formula: viability (%) = (A / B) × 100 %, where A stands for the number of CFUs observed post-treatment, and B denotes the number of CFUs in the control sample.

2.14. Transwell assays

In the upper chambers of transwell 24-well plates (Costar, Pore size 8.0 μ m, USA), 5 × 10^4 human umbilical vein endothelial cells (HUVECs) were seeded in cell culture medium without FBS. The lower chambers were filled with 600 μL of medium containing FBS. Following 24 h of incubation, cells were washed thrice with PBS, fixed in 4 % paraformaldehyde for half an hour, and subsequently stained with 0.5 % crystal violet for 30 min. Cells that did not invade or migrate were removed using fresh cotton swabs. Each well was examined under a bright field microscope, with three random fields captured. In order to assay the transwell ability of RAW264.7 with different treatments, 1 ×

10^5 RAW264.7 cells were plated in the upper chambers of transwell system while the medium of upper chamber was without FBS and the low chamber contained 20 % FBS. The cells were washed, fixed and stained to observe the number of the migrated cells with a bright field microscope.

2.15. Flow cytometric analysis

To investigate the potential impact of hydrogels on the M2 polarization of macrophages, RAW264.7 cells were exposed to hydrogels for 24 h. Subsequently, the cells underwent PBS washing and were stained with antibodies targeting CD11b and CD206 (BioLegend). After a 30-minute incubation at 4 °C, the cells were rinsed two times with PBS. Subsequently, the cytometric investigation was performed utilizing a BD Accuri C6 Plus flow cytometer (Becton Dickinson, Franklin Lakes, NJ, USA), and the information was assessed utilizing FlowJo software.

2.16. Lipidomics

After seven days of inducing adipogenic differentiation, dFBs were divided into two groups, each containing six sections. The experimental group was treated with FA. Following 48 h of treatment, the cells were collected, washed three times, and 50 mg samples were obtained from each group (cell count: 10^{-7}). Subsequently, 400 μL of methyl *tert*-butyl ether (MTBE), 80uL of methanol (MeOH), and 200 μL of water were added. After vortexing, sonication, and centrifugation, the upper MTBE phase was dried using N_2, followed by redissolving in 100 μL of dichloromethane (DCM):MeOH (1:1, v/v). The sample extracts underwent analysis using a UPLC – Orbitrap-MS system (UPLC, Vanquish; MS, HFX). High-resolution mass spectrometry (HRMS) data were acquired with a Q Exactive HFX Hybrid Quadrupole Orbitrap mass spectrometer, utilizing Full-ms-ddMS2 MS acquisition methods. The original MS data were obtained using Xcalibur 4.1 on the Q-Exactive instrument.

The analysis of data utilized the R package, which encompasses a variety of multivariate data analysis methods, including principal component analysis (PCA) and orthogonal partial least-squares discriminant analysis (OPLS-DA). In the OPLS-DA model, the variable importance in the projection (VIP) score for each variable was calculated to assess its significance in classification tasks. Metabolites that presented VIP values greater than 1 were subjected to a Student's *t*-test on a univariate basis to assess their significance. Metabolites were deemed statistically significant if their p-values were less than 0.05.

2.17. In vitro cytotoxicity

HUVECs were plated at a density of 2×10^3 cells per well in 96-well dishes and incubated in DMEM/F12 medium supplemented with 10 % FBS at 5 % CO_2 and 37 °C. The viability of HUVECs co-cultured with hydrogel membranes was determined using the CCK-8 kit (Life-iLab, China) on days 1, 2 and 3. The cells were incubated with 100 μL cultures containing 10 μL CCK-8 reagent for 2 h. Then the absorbance was recorded using a VICTOR Nivo multimode plate reader (PerkinElmer, Waltham, MA, USA). Furthermore, the viability of HUVECs was assessed using a calcein-FITC/PI live-dead staining kit (Solarbio, Beijing, China). The cells were washed 3 times and incubated with live-dead staining kit for 1 h. Finally, the cells were photoed with a fluorescence microscope (Olympus).

2.18. Hemolysis test

In order to assess the blood compatibility of the developed hydrogels, a hemolysis assay was performed. Initially, red blood cells (RBCs) were isolated from fresh blood of healthy SD rats by centrifugation at 2000 rpm for 10 min. Subsequently, 100 μL of different hydrogels, PBS (as a control group) and distilled water (as a positive control) were mixed with 500 μL of RBC suspension and incubated at 37°C for 12 h. After the incubation period, the supernatants were collected by centrifugation, and the optical density at 541 nm was measured.

2.19. Scratch assay

HUVECs were plated into 12-well culture plates and allowed to reach 90–100 % confluence. A sterile 200 μL pipette tip was used to create a straight-line scratch on the cell surface. Floating cells were removed with PBS. The images were collected at 0 h, 12 h and 24 h using a fluorescence microscope (Olympus).

2.20. ROS detection

HUVECs were seeded in 96-well plates at a density of 2×10^4 cells per well and exposed to 0.5 mM H_2O_2 along with various hydrogels for 8 h. The control group of HUVECs was treated with PBS. Intracellular ROS levels were evaluated by staining the cells with a DCFH-DA probe (Beyotime, Beijing, China) and imaging was performed using a microscope (Olympus).

2.21. Tube formation assay

The Matrigel (Corning, NY, USA) was placed in 96-well dishes and then the dishes were placed in an incubator at 37 °C for 45 min to turn the matrix glue into a solid. HUVECs with different treats were seeded at a density of $2 \times 10^{\hat{}}4$ cells per well in the 96-well dishes. The cells were further incubated for 6 h. Finally, three randomly selected fields were observed under a microscope, and the results were quantified using Image J software.

2.22. Generation of DIO mice

The research involving animals was reviewed and approved by the Institutional Animal Care and Use Committee of Tongji Medical College, Huazhong University of Science and Technology. The diet-induced obesity (DIO) mice were established in 6-week-old male C57BL/6J mice by feeding them a high-fat diet (HFD = 60 % calories from fat) for 12 weeks. The mice were weighed weekly.

2.23. Infected wound model

The mice were anesthetized using intraperitoneal pentobarbital sodium at a dosage of 50 mg/kg of body weight, obtained from Sigma Aldrich, prior to the creation of 1.0 × 1.0 cm full-thickness excision skin wounds. Following the excision, each wound was infected with 30 μL suspension of S. aureus, containing $3 \times 10^{\hat{}}8$ CFU/ml, for a duration of 10 min. Both normal and DIO mice were randomly assigned into three treatment groups: one treated with 100 μL of PBS, another with Ni@HA hydrogel, and the third with FA@Ni@HA hydrogel, with each group comprising five mice. Subsequently, the wounds were bandaged using gauze, and photographs were taken on days 0, 3, 7, 10 and 14 to monitor the healing process. The extent of wound closure was quantitatively assessed using ImageJ software. The degree of closure was calculated with the formula: $Cn = (A0 - An) / A0 \times 100\ \%$, where Cn indicates the percentage reduction of the wound area on specific days, A0 represents the initial wound size, and An is the wound area measured on the corresponding day after the injury.

2.24. HE staining and Masson staining

The wound tissues were initially fixed in a 4 % paraformaldehyde solution to preserve the tissue architecture and cellular components. Following fixation, the tissues were embedded in paraffin to facilitate slicing into ultra-thin sections. These sections were precisely cut to a thickness of 4 μm to ensure detailed microscopic analysis. The prepared sections were then subjected to staining using either Hematoxylin and

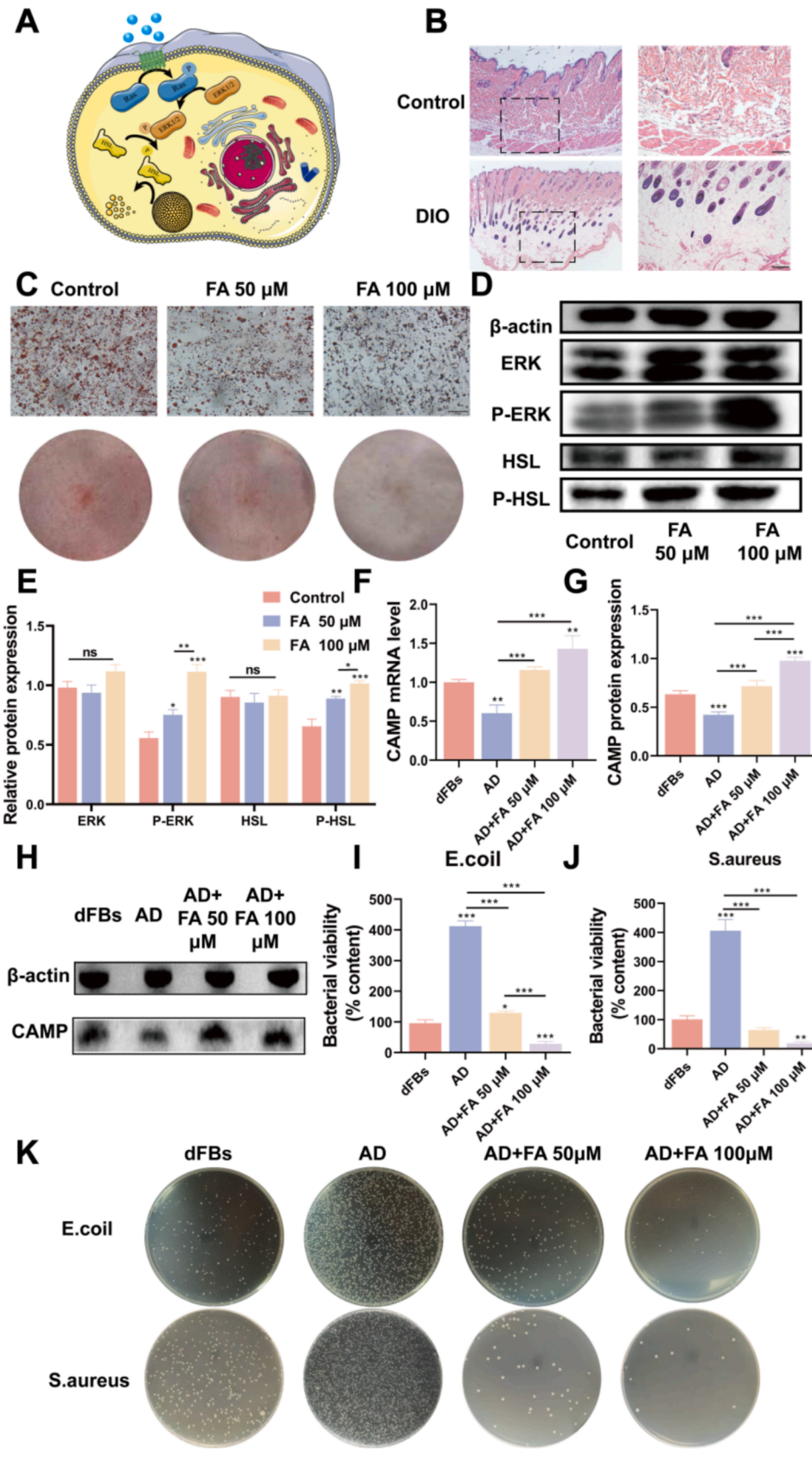

(caption on next page)

Fig. 2. The impact of FA on mature adipocytes. A) The mechanism through which FA enhances lipolysis. B) Hematoxylin-eosin (HE) staining observed the subcutaneous fat thickness in normal and DIO mice. Scale bar = 100 μm. C) Oil Red O staining assessed lipid droplet size in adipocytes. Scale bar = 50 μm. D, E) Western blot analysis of associated proteins (including ERK, p-ERK, HSL, and p-HSL) of mature adipocytes after different treatments. F) qRT-PCR expression of CAMP gene in dFBs after co-culture. G, H) Western blot analysis of CAMP protein in dFBs after co-culture. I-K) The number of colonies in each group was observed and corresponding quantitative analysis was performed. (*P < 0.05, **P < 0.01, ***P < 0.001). (For interpretation of the references to colour in this figure legend, the reader is referred to the web version of this article.)

Eosin (H&E) or Masson's trichrome staining techniques, each providing distinct histological information. Finally, the images were collected using an inverted microscope (Olympus).

2.25. Histological analysis

On the 14th day, the mice were euthanized, and the tissue from the wounds was preserved in paraffin and dyed. Retrieval of the antigen took place for a duration of 15 min in citrate buffer, with the subsequent 30 min being dedicated to blocking with goat serum. Later, the samples were dyed with anti-CD31, anti-VEGF, or anti-CD206 antibodies for a full night at a temperature of 4 °C, washed with PBS, and then dyed with DAB and hematoxylin respectively. Microvascularization at the wound sites was analyzed by tallying the amount of $CD31^+$ cells and examining the VEGF expression through a microscope. For the determination of M2 polarization, the count of $CD206^+$ cells was used. To evaluate the

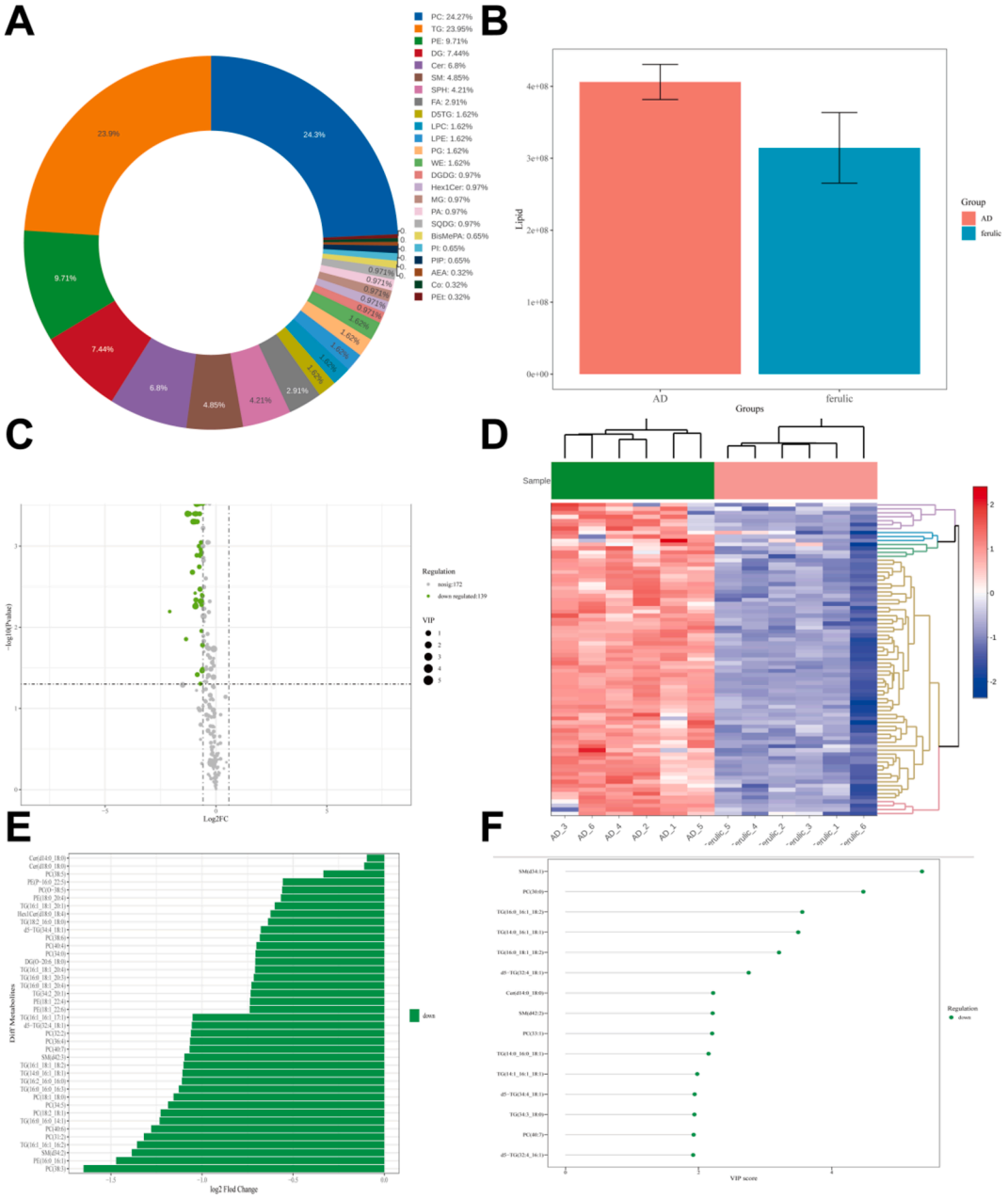

Fig. 3. Lipidomics results of mature adipocytes after FA treatment. A) Diagram of lipid subclass composition in mature adipocytes. B) Difference diagram of the total expression content of lipid molecules in the two groups. C) Lipid metabolite clustering heat map. D) Volcano plot of differential lipid metabolites. E) Bar graph of fold differences in differential lipid molecules. F) VIP score plot of differential lipid molecules.

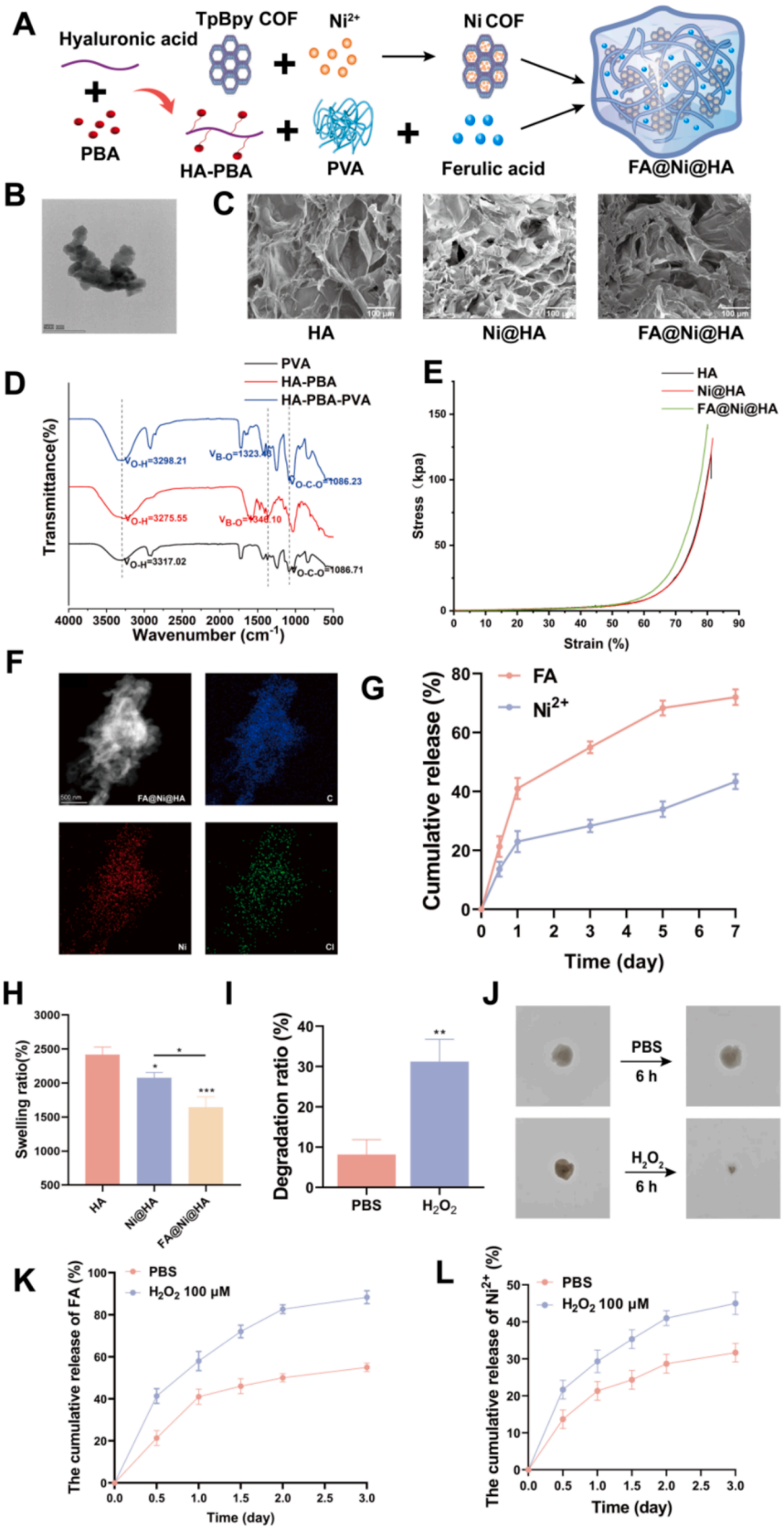

Fig. 4. Material characterization of FA@Ni@HA hydrogel. A) Schematic diagram of the synthesis of FA@Ni@HA hydrogel. B) The TEM images of the Ni COF. C) SEM image of FA@Ni@HA hydrogel. Scale bar = 100 μm. D) FT-IR spectrum of HA-PBA-PVA hydrogel. E) Compressive strain–stress curve of FA@Ni@HA hydrogel. F) EDX images of FA@Ni@HA hydrogel. G) The release test of FA and Ni^{2+} in FA@Ni@HA hydrogel. H) Swelling ratio of FA@Ni@HA hydrogel. I, J) ROS responsiveness of FA@Ni@HA hydrogel. K, L) The release test of FA and Ni^{2+} in the conditions of PBS or H_2O_2. (*P < 0.05, **P < 0.01, ***P < 0.001).

antibacterial ability, immunofluorescence staining was conducted based on the CAMP expression.

2.26. Statistical analysis

The findings were expressed as the mean plus or minus the standard deviation (SD). For the statistical examination, Student's *t*-test was deployed when comparing two distinct groups. In instances where comparisons involved more than two groups, ANOVA complemented by Tukey's post hoc test was employed. To ascertain statistical significance, a threshold of $p < 0.05$ was established.

3. Results and discussion

3.1. FA enhanced lipolysis through the ERK-HSL axis and stimulated the secretion of AMPs

The process by which FA boosts lipolysis is illustrated in Fig. 2A. Initially, we compared subcutaneous adipocytes in normal mice and DIO mice, revealing a notable increase in subcutaneous adipocytes in DIO mice (Fig. 2B). To determine the appropriate concentration of FA, a CCK-8 experiment was conducted, demonstrating no cytotoxic effects within the 10–200 μM range (Fig. S1). Subsequently, concentrations of 50 μM and 100 μM were selected for further experiments. To investigate the lipolysis promotion by FA, adipogenic differentiation of dFBs was induced for 14 days, followed by a two-day treatment with FA. Oil Red O staining indicated a significant increase in lipolysis post-FA treatment, with a noticeable reduction in lipid droplets under microscopic examination (Fig. 2C). Western blot was utilized to identify protein alterations in mature adipocytes. Fig. 2D, F illustrated a significant increase in the phosphorylation of ERK and HSL in the experimental group. Subsequent analysis with a free fatty acid detection kit revealed a rise in free fatty acid levels following FA treatment (Fig. S2). Building upon these findings, we investigated the impact on AMP cathelicidin (CAMP) secretion post lipolysis promotion. dFBs were placed in the upper chamber layer and induced lipogenic differentiation for 14 days, followed by the addition of FA for 48 h. Afterwards, the primary dFBs were placed in the lower chamber layer of the co-culture system (Fig. S3). Subsequently, cells and culture medium from the lower layer were collected. Western blot and qRT-PCR results demonstrated a reduction in CAMP secretion in the mature adipocytes group (AD), while treatment with FA significantly enhanced this secretion (Fig. 2F–H). In vitro antibacterial assays further confirmed the inhibitory effect on bacterial growth exhibited by the experimental group's culture medium (Fig. 2I–K). We investigated the dose-dependent antibacterial effects of FA. The results indicated that the MIC90 value for S.aureus is 60 μM, while the MIC90 value for E.coli is 40 μM (Fig. S4).

The Wounds of obesity mice are susceptible to bacterial infection, leading to delayed wound healing or worsening of the wound. Due to the overuse of antibiotics, drug-resistant bacteria are on the rise, highlighting the crucial need for alternative antibacterial methods. AMPs represent a novel class of antibacterial agents against various microbial pathogens, including both Gram-positive and Gram-negative bacteria [36]. These peptides have been utilized in the treatment of infected wounds [37–39]. For example, Wang et al. formed a collagen hydrogel loaded with AMPs as an antimicrobial wound dressing, showing excellent antimicrobial function [40]. Moreover, Wang et al. also designed a network of pH-switchable antimicrobial nanofibers based on the mechanism of AMPs, which achieved synergistic biofilm eradication and subsequent activation of the cell proliferation and healing cascade [41]. However, they may have limitations such as short duration of action, non-specific uptake, and potential effects on normal tissues. Therefore, it is highly important to locally stimulate the production of antibacterial peptides in infected wounds. Adipocytes, situated at the base of the dermis, serve as a key defense mechanism for the skin barrier [42]. They secrete AMPs to combat microorganisms such as S.aureus. In obesity models, however, mature adipocytes suppress the secretion of AMPs during wound infection [11]. FA was shown to activate the ERK pathway, leading to the phosphorylation of HSL and promotion of lipolysis. Our research demonstrated that by enhancing fat metabolism, dFBs regained their ability to secrete AMPs. Therefore, FA can enhance the local antibacterial function of the wound by stimulating the secretion of AMPs, thereby creating a conducive environment for infected wound healing.

3.2. Lipidomics showed that the lipid components in adipocytes changed significantly after FA treatment

To further explore the impact of FA on mature adipocytes, lipidomics was conducted to assess changes in adipocytes post-FA treatment. The results revealed significant alterations in the relevant lipid components within the cells. Fig. 3A illustrated the distribution of intracellular lipid components, with the top five being Phosphatidylcholine (PC), Triglyceride (TG), Phosphatidylethanolamine (PE), Diglyceride (DG), and Ceramide (Cer). Analysis of the overall lipid expression in Fig. 3B indicated that FA decreased the total lipid content in mature adipocytes. The heatmap results in Fig. 3C demonstrated shifts in metabolism-related lipids such as Cer, Sphingomyelin (SM), PC, TG, PE, Phosphatidylinositol (PI) and DG, which play roles in membrane component, energy storage and metabolism, as well as signal transduction and other functions [43]. Studies have indicated a close relationship between Cer and adipocytes metabolism. In diabetic adipocytes, decreasing intracellular Cer levels has been shown to boost mitochondrial metabolism and drive macrophage differentiation towards an anti-inflammatory phenotype [44,45]. Therefore, the alterations in adipocyte function following FA treatment may be linked to Cer levels. The subsequent volcano plot (Fig. 3D) demonstrated that FA treatment led to a decrease in various lipids in adipocytes, highlighting the role of FA in lipid metabolism. Fig. 3E, F further illustrated that FA treatment altered lipid components associated with membrane components, energy metabolism, and signal transduction. Both Fold Change Analysis and Variable Importance for the Projection (VIP) revealed significant effects of Cer. The differential expression of Cer and its underlying mechanisms warrant further investigation.

3.3. Material characterization of FA@Ni@HA hydrogel

Due to the obvious enhancement of ROS in the infected wounds, we designed FA@Ni@HA hydrogel (Fig. 4A). We designed a hyaluronic acid molecule with a high concentration of phenylboronic acid groups by reaction with PBA. This modified hyaluronic acid (HA-PBA) then reacted with PVA to form a phenylboronic acid ester bond (Fig. S5, S6). This modification allows for a rapid response of the hydrogel to infected wounds, facilitating the release of FA and Ni^{2+} to aid in controlling and promoting the healing process (Fig. S7). The morphology of Ni COF was examined using a transmission electron microscope (TEM) (Fig. 4B). The water absorption and response rate of hydrogels are closely linked to their porosity, which in turn affects transport resistance. The TEM images (Fig. 4C) revealed a continuous pore network in the surface morphology of the FA@Ni@HA hydrogel, highlighting its water absorption capabilities. Additionally, Fourier transform infrared spectroscopy (FT-IR) analysis of HA-PBA, PVA, and HA-PBA-PVA was conducted to detect any chemical reactions between the components (Fig. 4D). In the HA-PBA spectrum, the absorption peak at 1346.10 cm^{-1} corresponds to the BO bond, indicating successful grafting of phenylboronic acid onto HA. The PVA spectrum showed an absorption peak at 1086.71 cm^{-1} attributed to the CO bond, while in the HA-PBA-PVA spectrum, the peaks at 1323.43 cm^{-1} and 1086.23 cm^{-1} were associated with the BO bond and CO bond, revealing the cross-linking reactions between HA-PBA and PVA. The resistance of the FA@Ni@HA hydrogel under compression was assessed using cyclic compression tests. Fig. 4E illustrated that the FA@Ni@HA hydrogel exhibited a

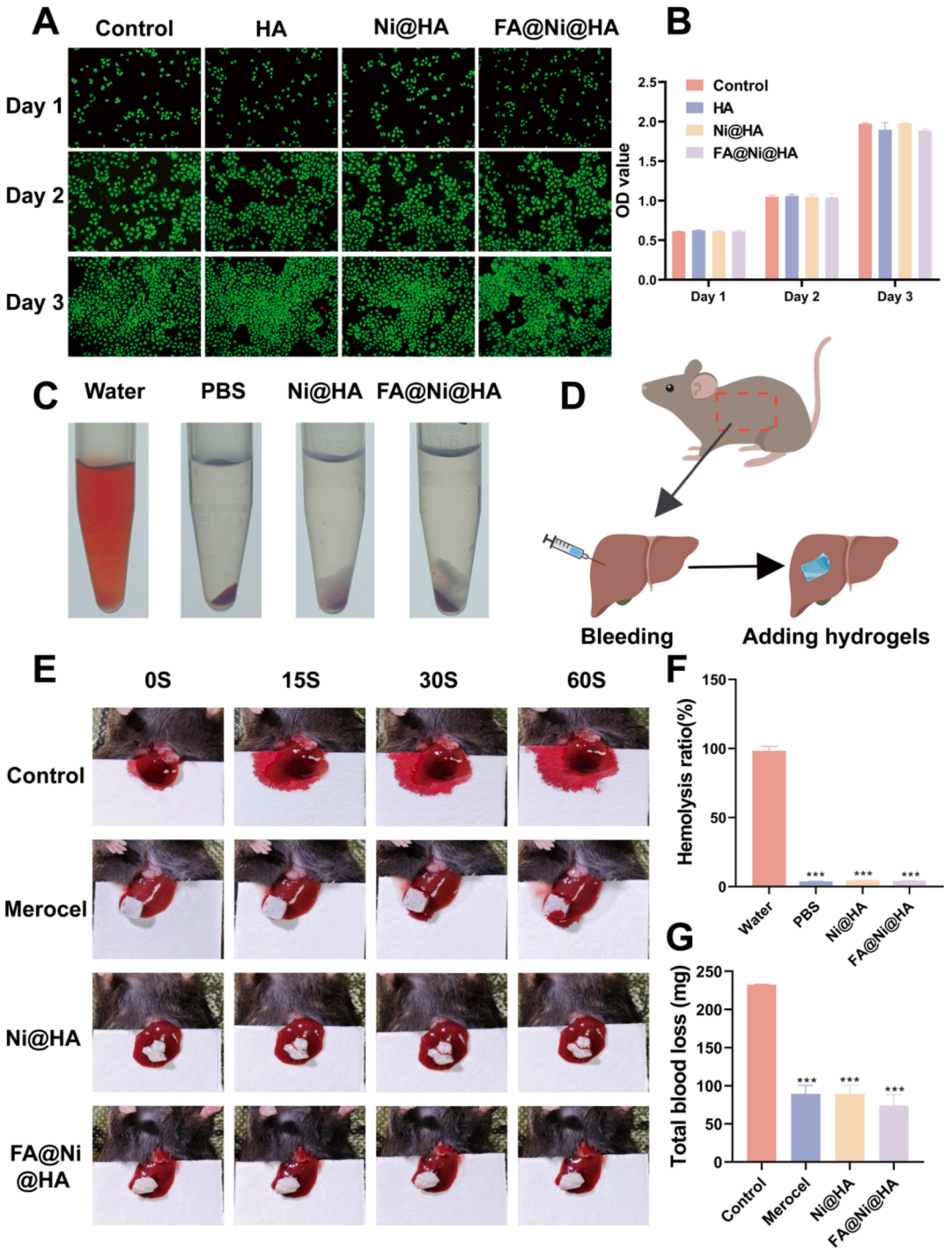

Fig. 5. Biocompatibility of FA@Ni@HA hydrogel. A) Live/dead staining of HUEVCs after treatment in each group. Scale bar = 100 μm. B) CCK-8 functional detection of HUVECs after FA@Ni@HA hydrogel treatment. C, F) Biocompatibility of FA@Ni@HA hydrogel toward red blood cells. D, E) Hemostatic properties of FA@Ni@HA hydrogel. G) Corresponding quantitative analysis of liver blood loss after FA@Ni@HA hydrogel treatment. (*P < 0.05, **P < 0.01, ***P < 0.001). (For interpretation of the references to colour in this figure legend, the reader is referred to the web version of this article.)

certain level of compressive strength, with the presence of COF nanoparticles not impacting the mechanical properties of the hydrogel. In order to observe the distribution of Ni^{2+}, energy dispersive X-ray (EDX) was subsequently employed to confirm the elemental composition of the FA@Ni@HA hydrogel (Fig. 4F, S8), demonstrating even distribution of the Ni^{2+} within the hydrogel.

The results of release test of FA and Ni^{2+} showed that the release of FA was much faster than Ni^{2+} (Fig. 4G). The ability of hydrogels to maintain a moist wound environment is essential for effective epidermal tissue repair. In this study, we evaluated the water absorption capacity of hydrogels by using a swelling ratio test (Fig. 4H). Results showed that FA@Ni@HA hydrogel could absorb more than 15 times its own weight in water. The interaction between ROS and phenylboronic acid ester bond can disrupt the network structure of the FA@Ni@HA hydrogel, leading to the release of FA and Ni^{2+}. Moreover, the FA@Ni@HA hydrogel showed rapid degradation in response to H_2O_2 concentration of 0.1 mM, demonstrating its sensitivity to oxidative stress (Fig. 4I, J). What's more, the release rate of FA or Ni^{2+} was significantly enhanced

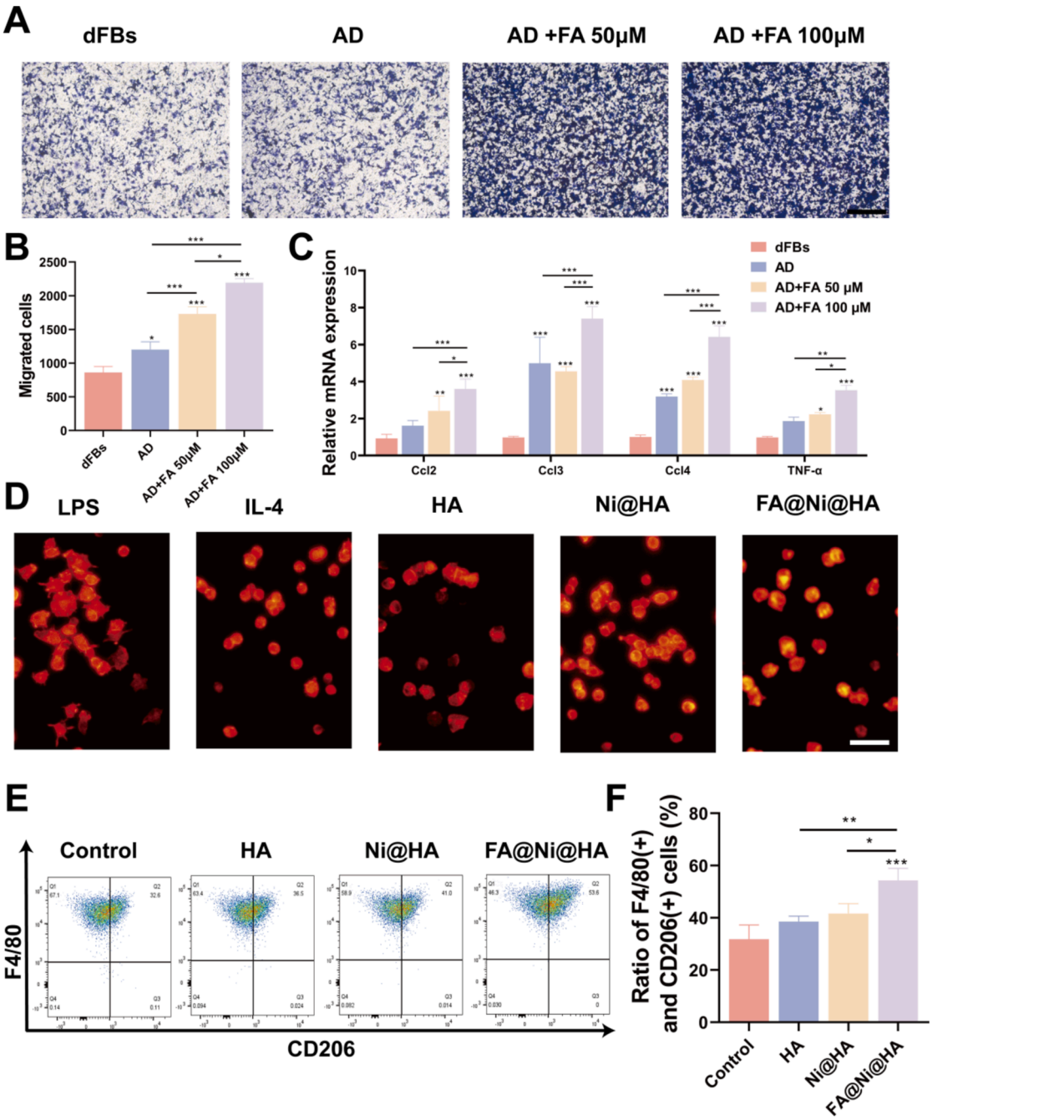

Fig. 6. Effect of FA on macrophage migration and FA@Ni@HA hydrogel on M2 macrophages. A,B) The culture medium of each group was co-cultured with RAW264.7 cells, and the migration ability of RAW264.7 cells was evaluated by transwell experiment. Scale bar = 100 μm. C) Expression of migration-related genes (Ccl2, Ccl3, Ccl4 and TNF-α) in RAW264.7 cells after different treatments. D) Cytoskeletal staining of RAW264.7 cells after different treatments. Scale bar = 50 μm. E, F) Flow cytometry and corresponding quantitative analysis of CD206 expression in RAW264.7 cells. (*P < 0.05, **P < 0.01, ***P < 0.001).

in H_2O_2 concentration of 0.1 mM, which may be related to the reaction of the phenyborate bond in FA@Ni@HA with ROS (Fig. 4K, L).

Excessive ROS during wound healing can trigger a robust inflammatory response, impede angiogenesis, and result in endothelial dysfunction [46]. In the presence of bacterial infection wounds, also reduced local nutrients and oxygen levels, heightened ROS production, and a deteriorating wound healing microenvironment could be observed [35]. When exposed to ROS, the FA@Ni@HA hydrogel degrades quickly and releases FA to exert its antioxidant properties. Hyaluronic acid, a crucial component of the extracellular matrix, offers outstanding biocompatibility and non-immunogenicity [47,48]. Moreover, hyaluronic acid possesses immunomodulatory and antioxidant capabilities due to its multiple functional groups, which are associated with enhanced tissue regeneration during wound healing [49]. Boric acid can readily form dynamic boronic acid ester bonds with 1,2-diol or 1,3-diol without the need for a catalyst, and has found widespread applications in tissue repair [50–52]. The application of Ni-doped biomaterials is limited by the potential toxicity of Ni^{2+}, which may lead to increased inflammation and oxidative damage [53]. Therefore, mitigating the toxicity of Ni^{2+} is crucial for enhancing the clinical applicability of Ni-doped materials. In this study, we incorporated Ni^{2+} into COF to facilitate a sustained and controlled release of Ni^{2+}. Additionally, FA within the hydrogel can help reduce inflammation and oxidative stress, thereby partially alleviating the toxicity of Ni^{2+}.

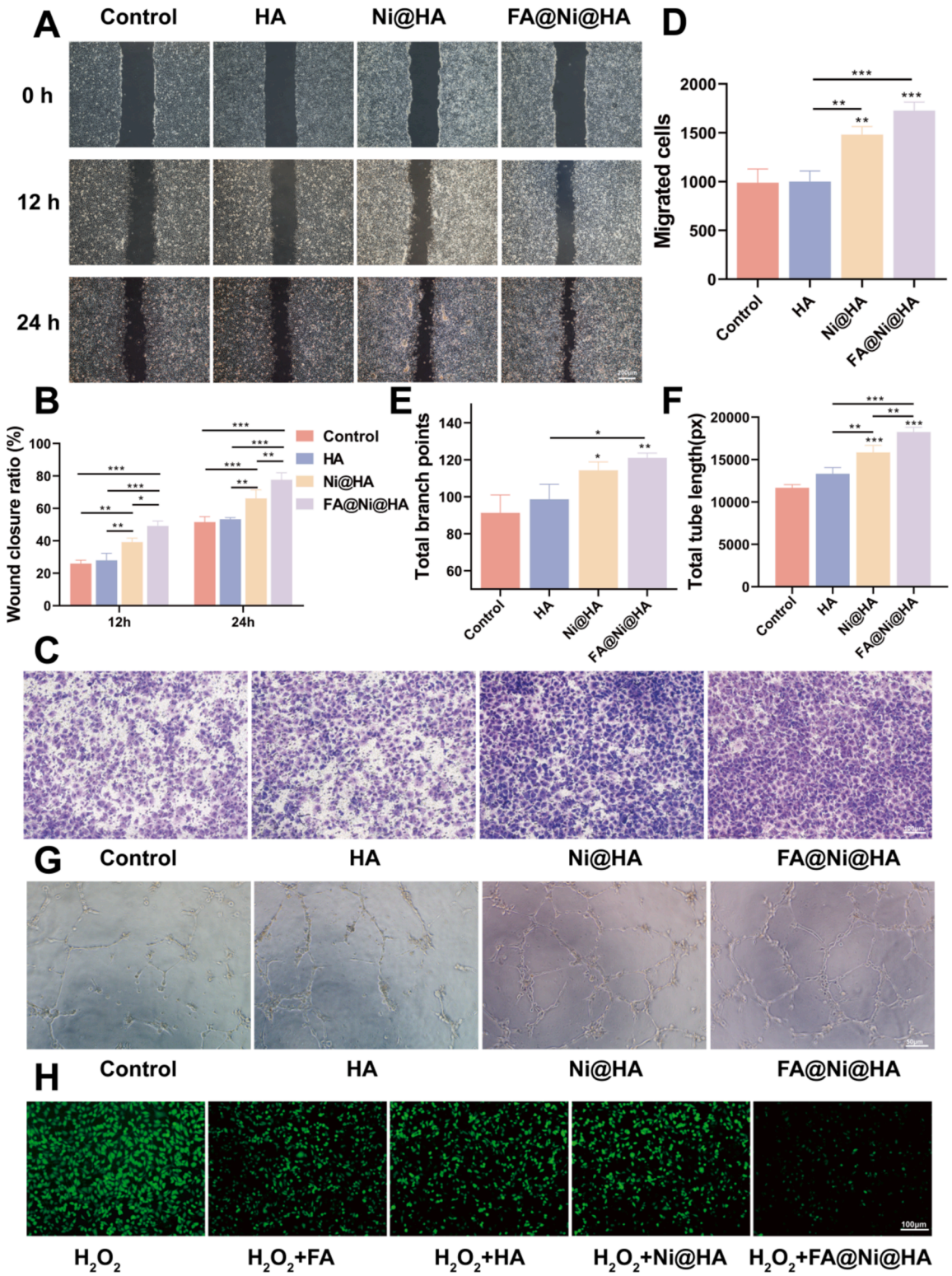

Fig. 7. Promotion of angiogenesis and antioxidant functions of FA@Ni@HA hydrogel. A, B) Scratch assays and corresponding quantitative analysis. Scale bar = 200 μm. C, D) Transwell assays to evaluate FA@Ni@HA hydrogel's promotion of HUVECs migration and corresponding quantitative analysis. Scale bar = 100 μm. E-G) Tube formation experiments and analysis of corresponding tube length and total branch points results. Scale bar = 50 μm. H) Fluorescent probe DCFH-DA performs ROS staining on HUVECs treated with FA@Ni@HA hydrogel, scale bar = 100 μm. (*P < 0.05, **P < 0.01, ***P < 0.001).

3.4. Favorable biocompatibility of FA@Ni@HA hydrogel

To assess the biocompatibility of FA@Ni@HA hydrogel, CCK-8 and live/dead assay were employed to examine its impact on HUVECs. Results indicated no significant differences among the four groups, demonstrating the favorable biocompatibility of FA@Ni@HA hydrogel (Fig. 5A, B). Furthermore, potential hemolysis of FA@Ni@HA hydrogel was assessed by co-culturing it with red blood cells of SD rats for 24 h, revealing hemolysis rates below 5 % for all groups with no evident hemolytic reactions observed (Fig. 5C, F). Subsequently, the hemostatic

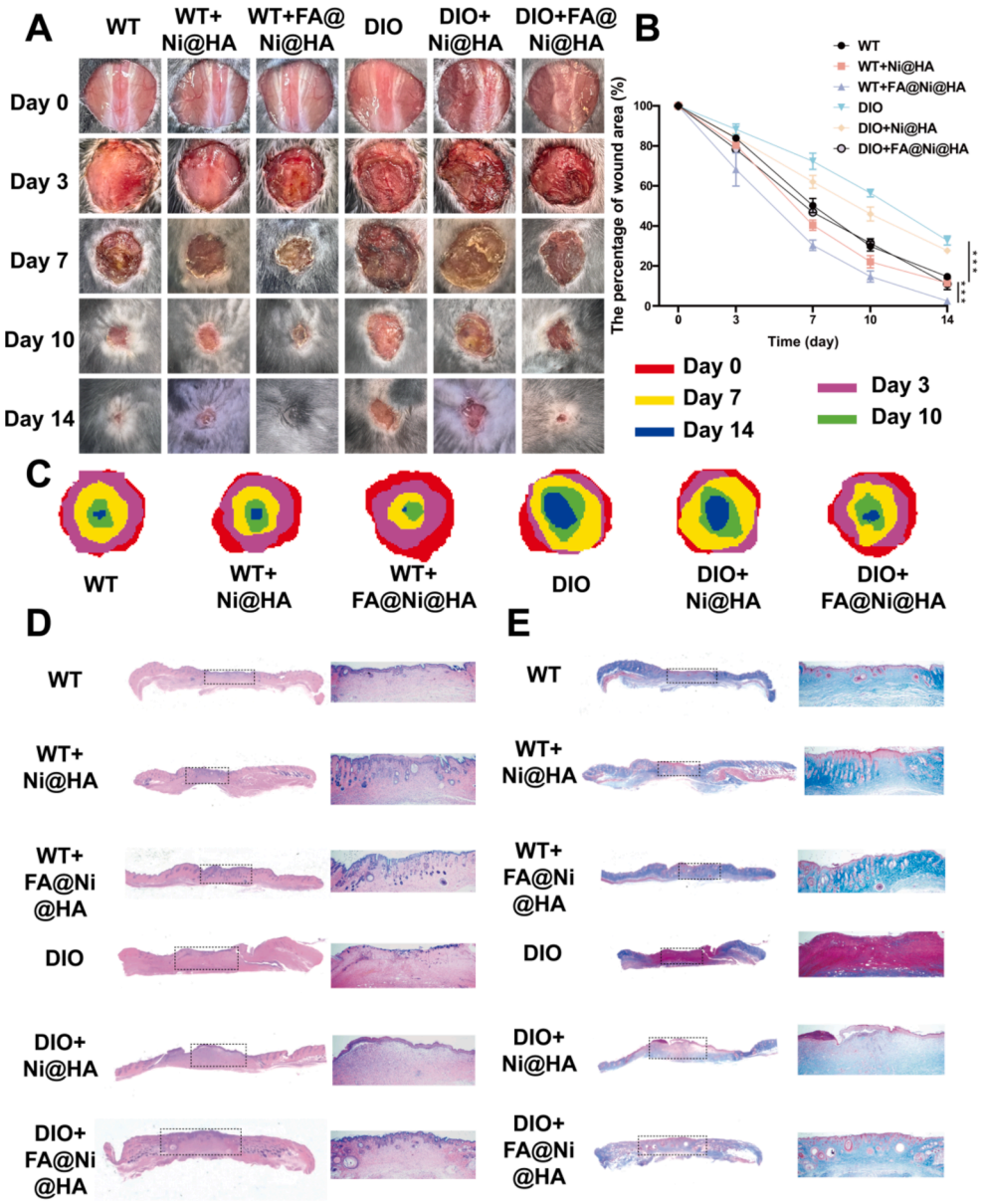

Fig. 8. FA@Ni@HA hydrogel promoted wound healing in vivo. A) Photographs of wounds of C57BL/6J mice after different treatments at different time points. B, C) Schematic representation of wound area and associated quantitative analysis. D) HE staining of tissue samples collected on day 14. Scale bar = 100 μm. E) Masson staining of tissue samples collected on day 14. Scale bar = 100 μm. (*P < 0.05, **P < 0.01, ***P < 0.001).

function of FA@Ni@HA hydrogel was assessed using a mouse bleeding model (Fig. 5D). The hydrogel notably reduced the amount of bleeding from the wound, possibly attributed to the bioadhesion and water absorption properties of FA@Ni@HA hydrogel (Fig. 5E, G). This dual functionality not only enables early hemostasis but also provides a robust protective barrier during the healing process of infected wounds.

3.5. FA enhanced the attraction of macrophages and the FA@Ni@HA hydrogel promoted the transformation of M2 macrophages

Studies have found that the lipolytic function of adipocytes is important for the recruitment of macrophages. To investigate the potential of FA in promoting macrophage recruitment, we treated RAW264.7 cells with the supernatant of mature fat cells treated with FA and observed their migration using transwell assays. The results revealed a significant increase in RAW264.7 cells migration in the experimental group, particularly following FA treatment (Fig. 6A, B). qRT-PCR analysis further confirmed these findings, showing upregulation of chemokine-related genes such as C-C motif chemokine ligand 2 (Ccl2), Ccl3, Ccl4, and tumor necrosis factor-α (TNF-α) in the experimental group (Fig. 6C). Notably, local inflammation can impede the wound healing process by preventing the transition to the proliferative phase, while FA possesses anti-inflammatory properties. Treatment of RAW264.7 cells with FA@Ni@HA hydrogel resulted in a morphology similar to that induced by IL-4 treatment, contrasting with the irregular shape observed in the LPS-treated group (Fig. 6D). Flow cytometry analysis demonstrated a significant increase in the proportion of $CD206^{+}$ cells following treatment with FA@Ni@HA hydrogel compared to the control group (Fig. 6E, F).

Silencing the ATGL gene, a pivotal enzyme in lipolysis, resulted in reduced macrophage recruitment [27], suggesting that fat cell-mediated macrophage recruitment may operate through lipolysis. We initially investigated the potential of adipocyte lipolysis to facilitate the recruitment of macrophages to infected wounds for antimicrobial purposes. The findings demonstrated that FA significantly enhanced the capacity of macrophage recruitment upon interaction with adipocytes.

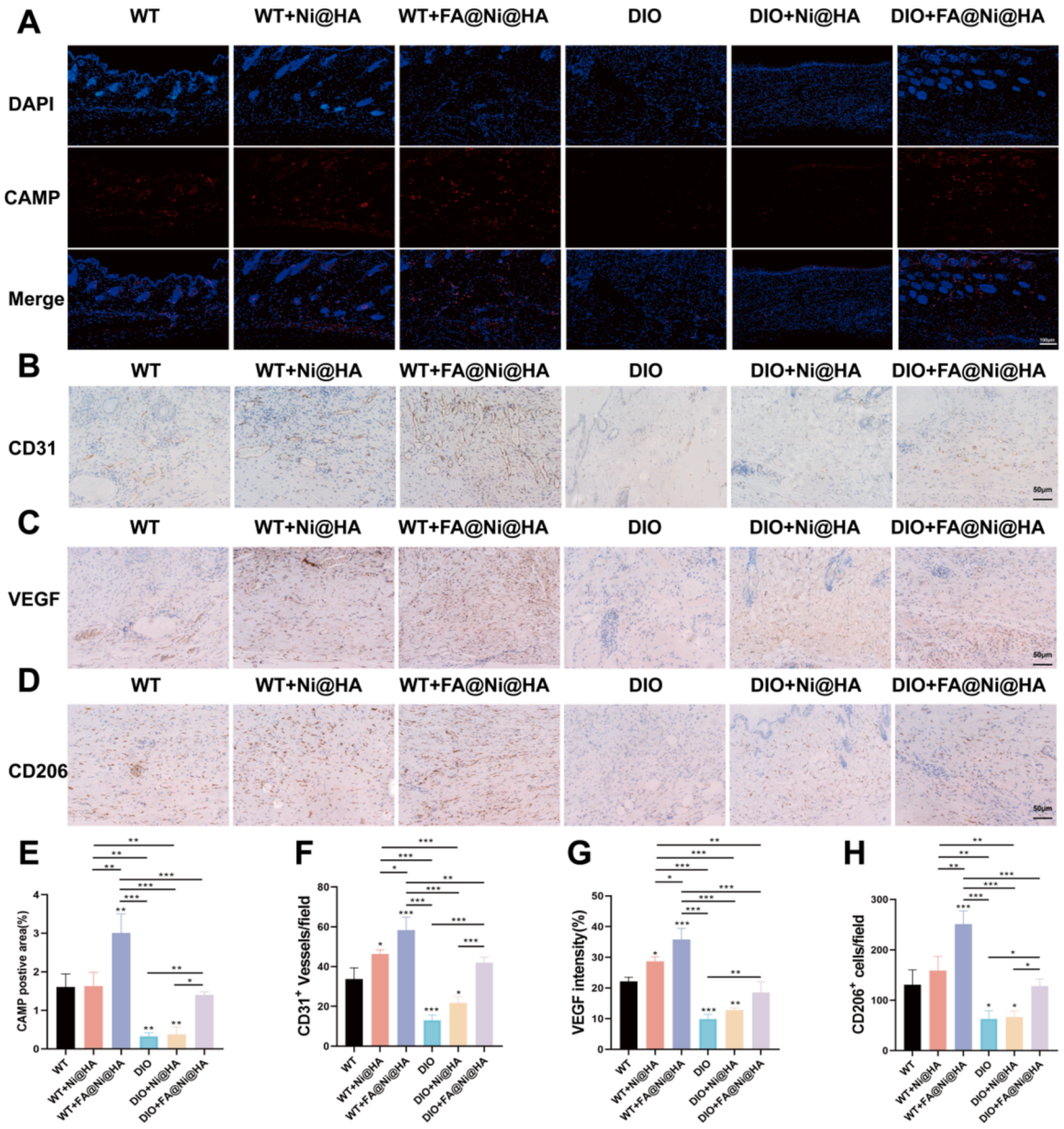

Fig. 9. FA@Ni@HA hydrogel promoted CAMP secretion, angiogenesis, and M2 cell polarization in vivo. A, E) Immunofluorescent staining of CAMP and corresponding quantification of the wounds on day 14. Scale bar = 100 μm. B, F) Immunohistochemical staining and quantification of $CD31^+$ vessels on day 14. Scale bar = 50 μ m. C, G) Immunohistochemical staining and quantification of VEGF were done on day 14. Scale bar = 50 μm. D, H) Immunohistochemical staining and quantitative analysis of CD206 were performed on day 14. Scale bar = 50 μm.(*P < 0.05, **P < 0.01, ***P < 0.001).

Macrophages play a crucial role in enhancing wound's anti-infection capabilities; however, an excessive and prolonged inflammatory response hampers transition into the proliferative stage and impairs wound healing. FA can promote the polarization of M2 macrophages which are vital for blood vessel regeneration and immune inflammation in the wound [54], thereby facilitating wound healing processes. In conclusion, our FA@Ni@HA hydrogel promoted both macrophage recruitment and the polarization of M2 macrophages, thereby achieving antimicrobial effects and tissue repair functions.

3.6. *The function of promoting angiogenesis and anti-oxidation of FA@Ni@HA hydrogel*

To investigate the impact of FA@Ni@HA hydrogel on angiogenesis, we conducted cell scratch assays to assess HUVECs migration following treatment with the hydrogels. Results demonstrated that both Ni@HA hydrogel and FA@Ni@HA hydrogel notably enhanced HUVECs migration, leading to a significant reduction in scratch gap (Fig. 7A, B). Particularly, FA@Ni@HA hydrogel exhibited the highest wound healing rate, possibly attributed to the synergistic effect of FA and Ni^{2+} in promoting HUVECs function. This finding was further supported by transwell assays as shown in Fig. 7C, D, indicating a significant increase of HUVECs in the FA@Ni@HA hydrogel group, facilitating early migration to the wound periphery. Subsequent assessment of FA@Ni@HA hydrogel's ability to stimulate HUVECs tube formation revealed a substantial increase in branching points and tube lengths in both Ni@HA hydrogel and FA@Ni@HA hydrogel groups (Fig. 7E–G), underscoring the hydrogel's efficacy in promoting HUVECs tube formation for improved oxygen and nutrient supply in the local microenvironment to support wound healing. Lastly, the antioxidant properties of the hydrogel were evaluated, showing a significant reduction in ROS content in HUVECs upon the addition of FA@Ni@HA hydrogel (Fig. 7H).

Angiogenesis plays a crucial role in the skin wound healing process by providing oxygen and nutrients to the wound area, thus promoting tissue regeneration [55]. HUVECs proliferate, migrate, and branch at the wound site during normal wound healing to establish novel blood vessels, ensuring the delivery of oxygen and essential nutrients [56]. Impaired angiogenesis in obesity is attributed to various factors, including alterations in inflammatory responses and ROS signaling [57]. Interestingly, our study discovered that FA@Ni@HA hydrogel significantly improved the blood vessel formation function of HUVECs compared to Ni@HA hydrogel. This suggests that FA may work in conjunction with Ni^{2+} to promote blood vessel formation.

3.7. FA@Ni@HA hydrogel's promotion of the healing of infected wounds in vivo

To investigate the potential of FA@Ni@HA hydrogel in accelerating the healing process of infected wounds, we conducted experiments using DIO mice and assessed the impact of the hydrogel on infected wound models. Our results, depicted in Fig. 8A–C, revealed that the FA@Ni@HA hydrogel group exhibited the highest rate of wound closure in wild type mice (WT). Conversely, DIO mice displayed the lowest healing rate, and the FA@Ni@HA hydrogel group in DIO mice demonstrated a significant enhancement in wound healing. Tissue samples were collected on day 14, followed by HE staining. Our analysis indicated that both normal mice and DIO mice treated with the FA@Ni@HA hydrogel displayed increased granulation tissue. Specifically, the FA@Ni@HA hydrogel group in the normal mice exhibited the most pronounced granulation tissue formation, whereas the DIO group showed a notable reduction in granulation tissue (Fig. 8D). Furthermore, Masson staining revealed that wounds treated with the FA@Ni@HA hydrogel in normal and DIO mice exhibited enhanced angiogenesis and collagen deposition, underscoring the significant role of the hydrogel in promoting wound healing (Fig. 8E).

3.8. Histological analysis

To investigate the potential of FA@Ni@HA hydrogel in antibacterial properties and promoting tissue repair in infected wounds, histological analysis was conducted across different experimental groups. Immunofluorescence analysis revealed that the expression of CAMP protein was notably higher in the FA@Ni@HA hydrogel group compared to other groups, indicating its efficacy in promoting CAMP secretion and enhancing resistance to wound infection (Fig. 9A, E). Furthermore, assessment of VEGF levels and $CD31^{+}$ vessels demonstrated a higher proportion of CD31 vessels (Fig. 9B, F) and increased VEGF levels (Fig. 9C, G) in wounds treated with FA@Ni@HA hydrogel, suggesting its ability to promote vascularization in infected wounds. Evaluation of M2 macrophages using CD206 expression showed a significant increase in M2 macrophages in wounds treated with FA@Ni@HA hydrogel (Fig. 9D, H). These findings collectively suggest that our hydrogel exhibits antibacterial properties, promotes wound healing, and enhances angiogenesis and M2 cell polarization in infected wounds.

Application of FA@Ni@HA hydrogel in infected wounds of obese mice significantly upregulated the expression of VEGF and the proportion of $CD31^{+}$ vessels. The accelerated wound healing observed in our study can be attributed to the multifaceted effects of the FA@Ni@HA hydrogel, which includes the controlled release of FA and Ni^{2+}, as well as its antibacterial, antioxidant, and pro-angiogenic properties. The hydrogel effectively absorbs wound exudate, maintains moisture, and creates an optimal environment for healing infectious wounds in obesity. Furthermore, the antibacterial and ROS-scavenging properties of the FA@Ni@HA hydrogel protect wounds from bacterial infections and ROS-induced damage, while also promoting M2 polarization and angiogenesis.

4. Conclusion

We presented a novel application of ROS-responsive FA@Ni@HA hydrogel for treating infectious wounds. The research demonstrated that FA promoted lipolysis and macrophage recruitment, leading to the secretion of AMPs and an antibacterial effect. The FA@Ni@HA hydrogel exhibited bioadhesive and water-absorbing properties, shielding the wound from external factors and providing effective antibacterial protection. The hydrogel's phenylboronic acid ester structure enables controlled drug release in response to ROS. Through the combined actions of FA and Ni^{2+} release, the hydrogel not only combats bacteria but also improves the wound environment, stimulates angiogenesis, and accelerates infected wound healing in vivo. Overall, the ROS-responsive FA@Ni@HA hydrogel offers a versatile therapeutic strategy to prevent infections, alleviate oxidative stress, and enhance angiogenesis during the healing process of infected wounds.

CRediT authorship contribution statement

Weixian Hu: Writing – original draft, Methodology, Conceptualization. **Yanzhi Zhao:** Methodology, Data curation, Conceptualization. **Shengming Zhang:** Writing – review & editing, Supervision, Methodology. **Yue An:** Writing – review & editing, Methodology, Data curation. **Samuel Knoedler:** Investigation, Funding acquisition. **Adriana Christine Panayi:** Investigation, Funding acquisition. **Doha Obed:** Methodology, Investigation. **Bong-Sung Kim:** Methodology, Investigation. **Kangkang Zha:** Supervision, Methodology. **Wenqian Zhang:** Methodology, Investigation. **Yixin Hu:** Methodology. **Bobin Mi:** Methodology. **Qian Feng:** Supervision, Funding acquisition. **Hankun Hu:** Supervision, Methodology. **Yun Sun:** Writing – review & editing, Supervision, Methodology. **Guohui Liu:** Writing – review & editing, Supervision, Funding acquisition.

Declaration of competing interest

The authors declare that they have no known competing financial interests or personal relationships that could have appeared to influence the work reported in this paper.

Acknowledgments

This work was supported by the National Science Foundation of China (No. 82272491, No. 82072444); Chinese Pharmaceutical Association Hospital Phamacy department (No. CPA-Z05-ZC-2022-002); Hubei Province Unveiling Science and Technology Projects (No. 2022-35); China Postdoctoral Science Foundation (No. 2023M731217).

Appendix A. Supplementary data

Supplementary data to this article can be found online at https://doi.org/10.1016/j.cej.2024.157300.

Data availability

No data was used for the research described in the article.

References

[1] P.A. Hirt, D.E. Castillo, G. Yosipovitch, J.E. Keri, Skin changes in the obese patient, J Am Acad Dermatol 81 (5) (2019) 1037–1057, https://doi.org/10.1016/j.jaad.2018.12.070.
[2] R. Huttunen, J. Syrjänen, Obesity and the outcome of infection, Lancet Infect. Dis. 10 (7) (2010) 442–443, https://doi.org/10.1016/S1473-3099(10)70103-1.
[3] R. Huttunen, J. Syrjänen, Obesity and the risk and outcome of infection, Int. J. Obes. (Lond) 37 (3) (2013) 333–340, https://doi.org/10.1038/ijo.2012.62.
[4] M.E. Falagas, A.P. Athanasoulia, G. Peppas, D.E. Karageorgopoulos, Effect of body mass index on the outcome of infections: a systematic review, Obes. Rev. 10 (3) (2009) 280–289, https://doi.org/10.1111/j.1467-789X.2008.00546.x.

[5] X. Zhao, H. Wu, B. Guo, R. Dong, Y. Qiu, P.X. Ma, Antibacterial anti-oxidant electroactive injectable hydrogel as self-healing wound dressing with hemostasis and adhesiveness for cutaneous wound healing, Biomaterials 122 (2017) 34–47, https://doi.org/10.1016/j.biomaterials.2017.01.011.

[6] Q. Wang, X. Liang, L. Shen, H. Xu, Z. Wang, C. Redshaw, Q. Zhang, Double Cross-Linked Hydrogel Dressings Based on Triblock Copolymers Bearing Antifreezing, Antidrying, and Inherent Antibacterial Properties, Biomacromolecules (2023), https://doi.org/10.1021/acs.biomac.3c01040.

[7] X. Lin, T. Fu, Y. Lei, J. Xu, S. Wang, F. He, Z. Xie, L. Zhang, An injectable and light curable hyaluronic acid composite gel with anti-biofilm, anti-inflammatory and pro-healing characteristics for accelerating infected wound healing, Int. J. Biol. Macromol. 253 (Pt 5) (2023) 127190, https://doi.org/10.1016/j.ijbiomac.2023.127190.

[8] M. Erdem Büyükkiraz, Z. Kesmen, Antimicrobial peptides (AMPs): A promising class of antimicrobial compounds, J Appl Microbiol 132(3) (2022) 1573-1596. 10.1111/jam.15314.

[9] A.A. Bahar, D. Ren, Antimicrobial peptides, Pharmaceuticals (Basel) 6 (12) (2013) 1543–1575, https://doi.org/10.3390/ph6121543.

[10] M.A. Mofazzal Jahromi, P. Sahandi Zangabad, S.M. Moosavi Basri, K. Sahandi Zangabad, A. Ghamarypour, A.R. Aref, M. Karimi, M.R. Hamblin, Nanomedicine and advanced technologies for burns: Preventing infection and facilitating wound healing, Adv Drug Deliv Rev 123 (2018) 33–64, https://doi.org/10.1016/j.addr.2017.08.001.

[11] L.-J. Zhang, C.F. Guerrero-Juarez, S.X. Chen, X. Zhang, M. Yin, F. Li, S. Wu, J. Chen, M. Li, Y. Liu, S.I.B. Jiang, T. Hata, M.V. Plikus, R.L. Gallo, Diet-induced obesity promotes infection by impairment of the innate antimicrobial defense function of dermal adipocyte progenitors, Sci. Transl. Med. 13 (577) (2021), https://doi.org/10.1126/scitranslmed.abb5280.

[12] L.-J. Zhang, C.F. Guerrero-Juarez, T. Hata, S.P. Bapat, R. Ramos, M.V. Plikus, R. L. Gallo, Innate immunity. Dermal adipocytes protect against invasive staphylococcus aureus skin infection, Science 347 (6217) (2015) 67–71, https://doi.org/10.1126/science.1260972.

[13] L.-J. Zhang, S.X. Chen, C.F. Guerrero-Juarez, F. Li, Y. Tong, Y. Liang, M. Liggins, X. Chen, H. Chen, M. Li, T. Hata, Y. Zheng, M.V. Plikus, R.L. Gallo, Age-related loss of innate immune antimicrobial function of dermal fat is mediated by transforming growth factor beta, Immunity 50 (1) (2019), https://doi.org/10.1016/j.immuni.2018.11.003.

[14] K. Arnke, P. Pfister, G. Reid, M. Vasella, T. Ruhl, A.-K. Seitz, N. Lindenblatt, P. Cinelli, B.-S. Kim, Impact of a High-Fat Diet at a Young Age on Wound Healing in Mice, Int. J. Mol. Sci. 24 (24) (2023), https://doi.org/10.3390/ijms242417299.

[15] G.F. Grabner, H. Xie, M. Schweiger, R. Zechner, Lipolysis: cellular mechanisms for lipid mobilization from fat stores, Nat Metab 3 (11) (2021) 1445–1465, https://doi.org/10.1038/s42255-021-00493-6.

[16] H. Lavoie, J. Gagnon, M. Therrien, ERK signalling: a master regulator of cell behaviour, life and fate, Nat. Rev. Mol. Cell Biol. 21 (10) (2020) 607–632, https://doi.org/10.1038/s41580-020-0255-7.

[17] A.K. Yadav, B.-C. Jang, Anti-adipogenic and Pro-lipolytic Effects on 3T3-L1 Preadipocytes by CX-4945, an Inhibitor of Casein Kinase 2, Int. J. Mol. Sci. 23 (13) (2022), https://doi.org/10.3390/ijms23137274.

[18] N.-J. Kim, J.-H. Baek, J. Lee, H. Kim, J.-K. Song, K.-H. Chun, A PDE1 inhibitor reduces adipogenesis in mice via regulation of lipolysis and adipogenic cell signaling, Exp. Mol. Med. 51 (1) (2019), https://doi.org/10.1038/s12276-018-0198-7.

[19] S. Maiti, B. Maji, H. Yadav, Progress on green crosslinking of polysaccharide hydrogels for drug delivery and tissue engineering applications, Carbohydr. Polym. 326 (2024) 121584, https://doi.org/10.1016/j.carbpol.2023.121584.

[20] Q. Ou, S. Zhang, C. Fu, L. Yu, P. Xin, Z. Gu, Z. Cao, J. Wu, Y. Wang, More natural more better: triple natural anti-oxidant puerarin/ferulic acid/polydopamine incorporated hydrogel for wound healing, J Nanobiotechnology 19 (1) (2021) 237, https://doi.org/10.1186/s12951-021-00973-7.

[21] P. Kuppusamy, S. Ilavenil, I.H. Hwang, D. Kim, K.C. Choi, Ferulic Acid Stimulates Adipocyte-Specific Secretory Proteins to Regulate Adipose Homeostasis in 3T3-L1 Adipocytes, Molecules 26 (7) (2021), https://doi.org/10.3390/molecules26071984.

[22] S. Franz, A. Ertel, K.M. Engel, J.C. Simon, A. Saalbach, Overexpression of S100A9 in obesity impairs macrophage differentiation via TLR4-NFkB-signaling worsening inflammation and wound healing, Theranostics 12 (4) (2022) 1659–1682, https://doi.org/10.7150/thno.67174.

[23] D. Merrick, P. Seale, Skinny Fat Cells Stimulate Wound Healing, Cell Stem Cell 26 (6) (2020) 801–803, https://doi.org/10.1016/j.stem.2020.04.021.

[24] S. Willenborg, D.E. Sanin, A. Jais, X. Ding, T. Ulas, J. Nüchel, M. Popović, T. MacVicar, T. Langer, J.L. Schultze, A. Gerbaulet, A. Roers, E.J. Pearce, J. C. Brüning, A. Trifunovic, S.A. Eming, Mitochondrial metabolism coordinates stage-specific repair processes in macrophages during wound healing, Cell Metab. 33 (12) (2021), https://doi.org/10.1016/j.cmet.2021.10.004.

[25] A.L. Mescher, Macrophages and fibroblasts during inflammation and tissue repair in models of organ regeneration, Regeneration (oxf) 4 (2) (2017) 39–53, https://doi.org/10.1002/reg2.77.

[26] S. Watanabe, M. Alexander, A.V. Misharin, G.R.S. Budinger, The role of macrophages in the resolution of inflammation, J. Clin. Invest. 129 (7) (2019) 2619–2628, https://doi.org/10.1172/JCI124615.

[27] B.A. Shook, R.R. Wasko, O. Mano, M. Rutenberg-Schoenberg, M.C. Rudolph, B. Zirak, G.C. Rivera-Gonzalez, F. López-Giráldez, S. Zarini, A. Rezza, D.A. Clark, M. Rendl, M.D. Rosenblum, M.B. Gerstein, V. Horsley, Dermal Adipocyte Lipolysis and Myofibroblast Conversion Are Required for Efficient Skin Repair, Cell Stem Cell 26 (6) (2020), https://doi.org/10.1016/j.stem.2020.03.013.

[28] L.-L. Zhou, Q. Guan, W. Zhou, J.-L. Kan, K. Teng, M. Hu, Y.-B. Dong, A Multifunctional Covalent Organic Framework Nanozyme for Promoting Ferroptotic Radiotherapy against Esophageal Cancer, ACS Nano 17 (20) (2023) 20445–20461, https://doi.org/10.1021/acsnano.3c06967.

[29] F. Yuan, C. Zhang, X. Luo, S. Cheng, Y. Zhu, Y. Xian, An erythrocyte membrane-camouflaged fluorescent covalent organic framework for starving/nitric oxide/immunotherapy of triple-negative breast cancer, Chem. Sci. 14 (48) (2023) 14182–14192, https://doi.org/10.1039/d3sc02022c.

[30] T. Dong, C. Duan, S. Wang, X. Gao, Q. Yang, W. Yang, Y. Deng, Multifunctional Surface with Enhanced Angiogenesis for Improving Long-Term Osteogenic Fixation of Poly(ether ether ketone) Implants, ACS Appl. Mater. Interfaces 12 (13) (2020) 14971–14982, https://doi.org/10.1021/acsami.0c02304.

[31] J. Liu, Z. Chen, H. Liu, S. Qin, M. Li, L. Shi, C. Zhou, T. Liao, C. Li, Q. Lv, M. Liu, M. Zou, Y. Deng, Z. Wang, L. Wang, Nickel-Based Metal-Organic Frameworks Promote Diabetic Wound Healing via Scavenging Reactive Oxygen Species and Enhancing Angiogenesis, Small 20 (10) (2024) e2305076.

[32] L. Zhang, Z. Liu, Q. Deng, Y. Sang, K. Dong, J. Ren, X. Qu, Nature-Inspired Construction of MOF@COF Nanozyme with Active Sites in Tailored Microenvironment and Pseudopodia-Like Surface for Enhanced Bacterial Inhibition, Angew. Chem. Int. Ed. Engl. 60 (7) (2021) 3469–3474, https://doi.org/10.1002/anie.202012487.

[33] Y. Li, L. Wang, H. Liu, Y. Pan, C. Li, Z. Xie, X. Jing, Ionic Covalent-Organic Framework Nanozyme as Effective Cascade Catalyst against Bacterial Wound Infection, Small 17 (32) (2021) e2100756.

[34] Y. Liang, J. He, B. Guo, Functional Hydrogels as Wound Dressing to Enhance Wound Healing, ACS Nano 15 (8) (2021) 12687–12722, https://doi.org/10.1021/acsnano.1c04206.

[35] T. Wang, Y. Li, E.J. Cornel, C. Li, J. Du, Combined Antioxidant-Antibiotic Treatment for Effectively Healing Infected Diabetic Wounds Based on Polymer Vesicles, ACS Nano 15 (5) (2021) 9027–9038, https://doi.org/10.1021/acsnano.1c02102.

[36] M. Magana, M. Pushpanathan, A.L. Santos, L. Leanse, M. Fernandez, A. Ioannidis, M.A. Giulianotti, Y. Apidianakis, S. Bradfute, A.L. Ferguson, A. Cherkasov, M. N. Seleem, C. Pinilla, C. de la Fuente-Nunez, T. Lazaridis, T. Dai, R.A. Houghten, R. E.W. Hancock, G.P. Tegos, The value of antimicrobial peptides in the age of resistance, Lancet Infect. Dis. 20 (9) (2020) e216–e230, https://doi.org/10.1016/S1473-3099(20)30327-3.

[37] G. Zhang, Y. Wang, H. Qiu, L. Lu, Facile one-pot synthesis of flower-like ellagic acid microparticles incorporating anti-microbial peptides for enhanced wound healing, J. Mater. Chem. B (2023), https://doi.org/10.1039/d3tb02016a.

[38] W. Hu, Z. Chen, X. Chen, K. Feng, T. Hu, B. Huang, J. Tang, G. Wang, S. Liu, G. Yang, Z. Wang, Double-network cellulose-based hybrid hydrogels with favourable biocompatibility and antibacterial activity for wound healing, Carbohydr. Polym. 319 (2023) 121193, https://doi.org/10.1016/j.carbpol.2023.121193.

[39] X. Mo, S. Zhao, J. Zhao, Y. Huang, T. Li, Y. Zhu, G. Li, Y. Li, H. Shan, Targeting collagen damage for sustained in situ antimicrobial activities, J. Control. Release 360 (2023) 122–132, https://doi.org/10.1016/j.jconrel.2023.06.013.

[40] X. Wang, D. Zhao, Y. Li, X. Zhou, Z. Hui, X. Lei, L. Qiu, Y. Bai, C. Wang, J. Xia, Y. Xuan, P. Jiang, J. Wang, Collagen hydrogel with multiple antimicrobial mechanisms as anti-bacterial wound dressing, Int. J. Biol. Macromol. 232 (2023) 123413, https://doi.org/10.1016/j.ijbiomac.2023.123413.

[41] J. Wang, X.-Y. Chen, Y. Zhao, Y. Yang, W. Wang, C. Wu, B. Yang, Z. Zhang, L. Zhang, Y. Liu, X. Du, W. Li, L. Qiu, P. Jiang, X.-Z. Mou, Y.-Q. Li, pH-Switchable Antimicrobial Nanofiber Networks of Hydrogel Eradicate Biofilm and Rescue Stalled Healing in Chronic Wounds, ACS Nano 13 (10) (2019) 11686–11697, https://doi.org/10.1021/acsnano.9b05608.

[42] O.A. Peña, P. Martin, Cellular and molecular mechanisms of skin wound healing, Nat. Rev. Mol. Cell Biol. (2024), https://doi.org/10.1038/s41580-024-00715-1.

[43] X. Han, Lipidomics for studying metabolism, Nat. Rev. Endocrinol. 12 (11) (2016) 668–679, https://doi.org/10.1038/nrendo.2016.98.

[44] B. Chaurasia, V.A. Kaddai, G.I. Lancaster, D.C. Henstridge, S. Sriram, D.L.A. Galam, V. Gopalan, K.N.B. Prakash, S.S. Velan, S. Bulchand, T.J. Tsong, M. Wang, M.M. Siddique, G. Yuguang, K. Sigmundsson, N.A. Mellet, J.M. Weir, P.J. Meikle, M.S. Bin M Yassin, A. Shabbir, J.A. Shayman, Y. Hirabayashi, S.-A.T.E. Shiow, S. Sugii, S.A. Summers, Adipocyte Ceramides Regulate Subcutaneous Adipose Browning, Inflammation, and Metabolism, Cell Metab 24(6) (2016) 820-834. 10.1016/j.cmet.2016.10.002.

[45] X. Zhang, Y. Zhang, P. Wang, S.-Y. Zhang, Y. Dong, G. Zeng, Y. Yan, L. Sun, Q. Wu, H. Liu, B. Liu, W. Kong, X. Wang, C. Jiang, Adipocyte Hypoxia-Inducible Factor 2α Suppresses Atherosclerosis by Promoting Adipose Ceramide Catabolism, Cell Metab. 30 (5) (2019), https://doi.org/10.1016/j.cmet.2019.09.016.

[46] J. Li, J. Zhang, P. Yu, H. Xu, M. Wang, Z. Chen, B. Yu, J. Gao, Q. Jin, F. Jia, J. Ji, G. Fu, ROS-responsive & scavenging NO nanomedicine for vascular diseases treatment by inhibiting endoplasmic reticulum stress and improving NO bioavailability, Bioact. Mater. 37 (2024) 239–252, https://doi.org/10.1016/j.bioactmat.2024.03.010.

[47] C. Qi, Q. Sun, D. Xiao, M. Zhang, S. Gao, B. Guo, Y. Lin, Tetrahedral framework nucleic acids/hyaluronic acid-methacrylic anhydride hybrid hydrogel with antimicrobial and anti-inflammatory properties for infected wound healing, Int. J. Oral Sci. 16 (1) (2024) 30, https://doi.org/10.1038/s41368-024-00290-3.

[48] Y. Zhan, Z. Zhou, M. Chen, X. Gong, Photothermal Treatment of Polydopamine Nanoparticles@Hyaluronic Acid Methacryloyl Hydrogel Against Peripheral Nerve Adhesion in a Rat Model of Sciatic Nerve, Int. J. Nanomed. 18 (2023) 2777–2793, https://doi.org/10.2147/IJN.S410092.

[49] Y. Liang, X. Zhao, T. Hu, B. Chen, Z. Yin, P.X. Ma, B. Guo, Adhesive Hemostatic Conducting Injectable Composite Hydrogels with Sustained Drug Release and Photothermal Antibacterial Activity to Promote Full-Thickness Skin Regeneration During Wound Healing, Small 15 (12) (2019) e1900046.
[50] X. Zhou, L. Dong, B. Zhao, G. Hu, C. Huang, T. Liu, Y. Lu, M. Zheng, Y. Yu, Z. Yang, S. Cheng, Y. Xiong, G. Luo, W. Qian, R. Yin, A photoactivatable and phenylboronic acid-functionalized nanoassembly for combating multidrug-resistant gram-negative bacteria and their biofilms, Burns, Trauma 11 (2023) tkad041, https://doi.org/10.1093/burnst/tkad041.
[51] P. Chakma, D. Konkolewicz, Dynamic Covalent Bonds in Polymeric Materials, Angew. Chem. Int. Ed. Engl. 58 (29) (2019) 9682–9695, https://doi.org/10.1002/anie.201813525.
[52] N. Lagneau, L. Terriac, P. Tournier, J.J. Helesbeux, G. Viault, D. Séraphin, B. Halgand, F. Loll, C. Garnier, C. Jonchère, M. Rivière, A. Tessier, J. Lebreton, Y. Maugars, J. Guicheux, C. Le Visage, V. Delplace, A new boronate ester-based crosslinking strategy allows the design of nonswelling and long-term stable dynamic covalent hydrogels, Biomater. Sci. 11 (6) (2023) 2033–2045, https://doi.org/10.1039/d2bm01690g.
[53] T. Khodaei, E. Schmitzer, A.P. Suresh, A.P. Acharya, Immune response differences in degradable and non-degradable alloy implants, Bioact. Mater. 24 (2023) 153–170, https://doi.org/10.1016/j.bioactmat.2022.12.012.
[54] P. Cheng, X. Xie, L. Hu, W. Zhou, B. Mi, Y. Xiong, H. Xue, K. Zhang, Y. Zhang, Y. Hu, L. Chen, K. Zha, B. Lv, Z. Lin, C. Lin, G. Dai, Y. Hu, T. Yu, H. Hu, G. Liu, Y. Zhang, Hypoxia endothelial cells-derived exosomes facilitate diabetic wound healing through improving endothelial cell function and promoting M2 macrophages polarization, Bioact. Mater. 33 (2024) 157–173, https://doi.org/10.1016/j.bioactmat.2023.10.020.
[55] S. Lyu, Q. Liu, H.-Y. Yuen, H. Xie, Y. Yang, K.-W.-K. Yeung, C.-Y. Tang, S. Wang, Y. Liu, B. Li, Y. He, X. Zhao, A differential-targeting core-shell microneedle patch with coordinated and prolonged release of mangiferin and MSC-derived exosomes for scarless skin regeneration, Mater. Horiz. (2024), https://doi.org/10.1039/d3mh01910a.
[56] J.-Y. Ding, M.-J. Chen, L.-F. Wu, G.-F. Shu, S.-J. Fang, Z.-Y. Li, X.-R. Chu, X.-K. Li, Z.-G. Wang, J.-S. Ji, Mesenchymal stem cell-derived extracellular vesicles in skin wound healing: roles, opportunities and challenges, Mil. Med. Res. 10 (1) (2023) 36, https://doi.org/10.1186/s40779-023-00472-w.
[57] C.E. Hagberg, K.L. Spalding, White adipocyte dysfunction and obesity-associated pathologies in humans, Nat. Rev. Mol. Cell Biol. 25 (4) (2024) 270–289, https://doi.org/10.1038/s41580-023-00680-1.